The Gounkoto Au deposit, West Africa: Constraints on ore genesis and volatile sources from petrological, fluid inclusion and stable isotope data

James S. Lambert-Smith, David M. Lawrence, Carlos A. Vargas, Adrian J. Boyce, Peter J. Treloar, Sarah Herbert

PII: S0169-1368(15)30153-0
DOI: doi: 10.1016/j.oregeorev.2015.10.025
Reference: OREGEO 1655

To appear in: *Ore Geology Reviews*

Received date: 31 May 2015
Revised date: 8 September 2015
Accepted date: 23 October 2015

Please cite this article as: Lambert-Smith, James S., Lawrence, David M., Vargas, Carlos A., Boyce, Adrian J., Treloar, Peter J., Herbert, Sarah, The Gounkoto Au deposit, West Africa: Constraints on ore genesis and volatile sources from petrological, fluid inclusion and stable isotope data, *Ore Geology Reviews* (2015), doi: 10.1016/j.oregeorev.2015.10.025

The Gounkoto Au deposit, West Africa: constraints on ore genesis and volatile sources from petrological, fluid inclusion and stable isotope data

James S. Lambert-Smith[1*], David M. Lawrence[2], Carlos A. Vargas[2], Adrian J. Boyce[3] Peter J. Treloar[1] and Sarah Herbert[2]

[1]School of Geography, Geology and the Environment, Kingston University London, Kingston upon Thames, KT1 2EE, UK

[2]Randgold Resources Ltd, Unity Chambers, Halkett Street, St Helier, Jersey, JE2 4WJ

[3]Scottish Universities Environmental Research Centre, East Kilbride, Glasgow, Scotland, G75 0QF

***Corresponding author email address: J.S.Lambert-Smith@kingston.ac.uk**

Abstract

The Loulo-Gounkoto complex in the Kédougou-Kéniéba Inlier hosts three multi-million ounce orogenic gold deposits, situated along the Senegal-Mali Shear Zone. This west Malian gold belt represents the largest West African orogenic gold district outside Ghana. The Gounkoto deposit is hosted to the south of the Gara and Yalea gold mines in the Kofi Series metasedimentary rocks. The ore body is structurally controlled and is characterised by sodic and phyllic alteration, As- and Fe-rich ore assemblages, with abundant magnetite, and overall enrichment in Fe-As-Cu-Au-Ag-W-Ni-Co-REE + minor Te-Pb-Se-Cd. Fluid inclusion analysis indicates that the deposit formed at P-T conditions of approximately 1.4 kbar and 340 °C and that two end member fluids were involved in mineralisation: (1) a moderate temperature (315-340 °C), low salinity (<10 wt. % NaCl equiv.), low density (≤1 gcm^{-3}), H_2O-CO_2-NaCl-H_2S±N_2-CH_4 fluid; (2) a high temperature (up to 445 °C), hypersaline (~40 wt. % NaCl equiv.), high density (~1.3 gcm^{-3}), H_2O-CO_2-NaCl±$FeCl_2$ fluid. Partial mixing of these fluids within the Jog Zone at Gounkoto enhanced phase separation in the aqueo-carbonic fluid and acted as a precipitation mechanism for Au. These findings demonstrate the widespread, if heterogeneously distributed, nature of fluid mixing as an ore forming process in the Loulo-Gounkoto complex, operating over at least a 30 km strike length of the shear zone. Stable isotope analyses of ore components at Gounkoto indicate a dominant metamorphic source for H_2O, H_2S and CO_2, and by extension Au. It thus can be reasoned that both the aqueo-carbonic and the hypersaline fluid at Gounkoto are of metamorphic origin and that the high levels of salinity in the brine are likely derived from evaporite dissolution.

Key Words

Gounkoto gold deposit; Fluid inclusions; stable isotopes; orogenic gold mineralisation; Birimian orogeny ; Senegal-Mali Shear Zone

1. Introduction

The Loulo-Gounkoto complex in Western Mali is situated along the Senegal-Mali Shear Zone and includes the Gara, Yalea and Gounkoto deposits as well as numerous satellites. With the Loulo Mine (Gara and Yalea deposits) to the north, the Gounkoto deposit is the third >3 Moz deposit to be discovered in the district since Gara in 1981. Gounkoto has a current reserve of 3.2 Moz @ 4.4 g/t, which combined with the Loulo reserve of 4.9 Moz @ 4.6 g/t gives the complex an overall reserve of 7.8 Moz. The Gounkoto discovery was announced in 2009 following an airborne electromagnetic survey of the region. Reconnaissance diamond drill holes intersected 46.6 m at 13.6 g/t, confirming Gounkoto as a significant new discovery and mining commenced in 2011. The Loulo-Gounkoto complex has produced over 3.5 Moz from open pit and underground resources, and has a current (2015) mining lifespan of 9 years at 660 Koz Au pa.

Lawrence et al., (2013a) detailed two separate end member styles of mineralisation for Au deposits at Loulo, encompassing Gara, Yalea, and numerous satellite deposits. Gara-style deposits feature: 1) pyrite as the dominant ore mineral; 2) tourmaline alteration and 3) REE-Ni-P-Zn-Se-Mo enrichment. Conversely Yalea-style ore bodies feature: 1) arsenopyrite as the dominant ore mineral; 2) albitisation and sericite-chlorite alteration assemblages and; 3) no enrichment in REE-Ni-P-Zn-Se-Mo. In addition, Lawrence (2013b) found that two distinct hydrothermal fluids were involved in mineralization at Loulo: 1) a high temperature, hypersaline aqueous fluid; and 2) a lower temperature, low salinity, CO_2-N_2-H_2S rich metamorphic fluid. The Gara deposit is interpreted to have formed as a result of partial mixing of these two fluids, whereas the Yalea deposit formed from unmixing of an immiscible, metamorphic sourced CO_2-rich fluid.

This paper will present new petrographic, fluid inclusion and stable isotope data from the Gounkoto deposit with the aim of comparing mineralisation processes and styles with those at Loulo. We will demonstrate that Au precipitation was initiated through a combination of fluid immiscibility in an aqueous-carbonic fluid and partial mixing of that same fluid with a hypersaline brine, processes described at the Gara and Yalea deposits by Lawrence et al., (2013b). Furthermore, we will examine the sources of volatile components in the deposit with a suite of stable isotope analyses conducted on ore components.

2. Regional Geology

The geology of the Birimian of West Africa is well documented (Abouchami et al., 1990; Liegois et al., 1991; Milési et al., 1992; Feybesse and Milesi 1994; Feybesse et al., 2006). This consists of NNE trending volcanic belts or arcs separated by broad metasedimentary basins intruded by voluminous granitic batholiths, and extends from the Ashanti belt in Ghana in the south east to the Kédougou-Kéniéba Inlier in the North West (Figure 1A). These arcs and basins were accreted, deformed and metamorphosed (greenschist facies) during the Eburnean orogeny ~2.1 Ga (Oberthür et al., 1998; Allibone et al., 2002; Feybesse et al., 2006). The Eburnean comprises three distinct phases of deformation (Liegois et al., 1991; Ledru et al., 1991; Hirdes and Davis, 1992; Feybesse et al., 2006; Dabo and Aifa, 2010; Dabo and Aifa 2011). Initial NW-SE compression (D_1) generated a penetrative S_1 cleavage parallel to recumbent F_1 fold axes. Subsequent sinistral strike-slip deformation (D_2), which cross cut and refolded S_1 cleavages, lead to the development of crustal scale shears along terrane boundaries. The latest phase of deformation is a brittle dextral strike-slip reactivation (D_3). D_1 occurred diachronously from SE to NW, between 2170 to 2096 Ma (Feybesse and Milési, 1994), when D_2 deformation began, continuing until 1980 Ma (Feybesse et al., 2006). Liegois et al., (1991) suggest that D3 began ~100Ma after D_2.

The Loulo-Gounkoto complex is the largest West African orogenic gold district outside Ghana, and is situated in the Kofi Series of the eastern Birimian Kédougou-Kéniéba Inlier (Figure 1B), which is bounded to the west by the Hercynian Mauritanide belt and unconformably overlain by flat lying Neoproterozoic sediments to the east. The inlier consists of two N- to NNE-trending greenstone belts, known as the Mako Series and Falémé Series, separated by two sedimentary basins; the Dialé-Daléma Series and the Kofi Series (Hirdes and Davis, 2002; Figure 1B). Loulo is situated within the West Mali gold belt, which stretches 180 km north-south along the Senegal border. Operational mines in the region include Gara and Yalea (at the Loulo Mine complex), Gounkoto, Sadiola, Yatela, Tabakoto, and Segala. These deposits are structurally controlled by a major crustal-scale lineament known as the Senegal-Mali shear zone (SMSZ; Figure 1B and C).

The Kofi Series rocks comprised of immature detrital sedimentary (dominantly quartzo-feldspathic wackes) and carbonate rocks (marbles and marls), and breccias, intruded by minor mafic dykes and small intermediate to felsic stocks. Some metaquartzwacke horizons have been intensely tourmalinized and others albitised (Lawrence et al., 2013a). Several extensive bodies of hydrothermal albitite are located close to the Senegal-Mali Shear Zone (Figure 1C). Igneous rocks comprising dykes of dolerite to monzodiorite composition and small stocks of quartz-feldspar-phyric rhyolite intrude the Kofi Series. In addition two larger plutons of monzogranite composition, the Gamaye and Yatea plutons, also intrude the south and east of the Series (Figure 1B and C).

3. Previous work on the Loulo-Gounkoto complex

Lawrence et al. (2013a and b) described in detail the Gara and Yalea deposits, situated to the north of Gounkoto (Figure 1C). At Gara, ore is hosted in ankerite-quartz-pyrite veins, developed in a fractured and folded quartz wacke unit that has previously been pervasively tourmalinized. Accessory ore phases at Gara include chalcopyrite, gersdorffite, pentlandite, arsenopyrite, monazite, scheelite and xenotime. Arsenopyrite is scarce in comparison to other orogenic gold deposits (Groves et al., 1998). The Yalea deposit is hosted in a 10- to 40-m-wide zone of strongly metasomatized (carbonate-albite followed by sericite-chlorite), brittle-ductile deformed rocks. In contrast to Gara, the Yalea Main ore body is As-rich. Arsenopyrite and arsenian pyrite are the dominant sulphide phases with accessory pyrrhotite, chalcopyrite and tennantite. Alteration assemblages lack tourmaline, but sodic, carbonate and phyllic alteration are widespread. Lawrence et al. (2013b) reported fluid inclusion assemblages at Gara representing two distinct fluids: 1) A high T, high-salinity, aqueous, CO_2-poor fluid (~400°C; ~45-55 wt. % NaCl equiv.; XH_2O of 0.7-0.8; XCO2 < 0.3); and 2) a lower T, low-salinity, H_2O-CO_2 fluid (270-350°C; <10 wt. % NaCl equiv.). High salinity fluid inclusions contain NaCl, $FeCl_2$, Fe_2O_3, Fe_3O_4 and carbonates as daughter minerals. Partial mixing occurred between these two fluids, which resulted in retrograde boiling and changes in the physico-chemical state of both fluids leading to Au precipitation. This is documented by the co-existence of H_2O-CO_2-NaCl inclusions of variable salinity and volatile compositions (Lawrence et al., 2013b). At Yalea Main the hypersaline fluid is notably absent and fluid inclusion assemblages are derived from phase separation in the low salinity H_2O-CO_2 fluid described at Gara.

4. Geology and structure of the Gounkoto deposit

The Gounkoto deposit is hosted on two left stepping jogs between a series of NNE trending sinistral shear zones, which developed during D_2 (Figure 2). Discrete N-S and NNW trending shears intersect the ore body along its ~2 km strike. This geometry is divided into five zones: 1) the Fe structure; 2) the wrench zone; 3) the pinch zone; 4) the jog zone; 5) the hanging wall ore body. The hanging wall comprises easterly-dipping, fine argillaceous sandstones, intercalated with dolostone units. Argillaceous sands are also present in the footwall, they dip steeply to the west and are interbedded with calcareous sandstone and phyllite. This sequence gives way to a metaquartzwacke unit. All units are intruded by numerous quartz monzodiorite dykes. The hanging wall and footwall are separated by a shear bounded package of strongly albitised metasedimentary rocks (Figure 2).

The southern part of the ore body consists of a hard linked sinistral dilational jog. Here, deformed and albitised rocks are bounded on the hanging wall by east dipping mineralised shear zones (354/70E) and west dipping shear zones in the footwall (184/84W). This jog represents the intersection between the long lived Fe structure, characterised by abundant Fe oxides and brittle D2 deformation overprinting earlier ductile deformation, and the Wrench Zone. A small subset of NNW trending shears (345/82WSW) in the wrench zone provide the linking architecture. North of this intersection the ore body narrows in to the Pinch Zone for ~500 m before making another 150-200 m left hand step-over in the Jog Zone. This step-over hosts the highest-grade mineralisation at Gounkoto and is a site of significant dilatancy and deformation. Discrete N-S (008/85 E) trending shear zones host three en-echelon ore bodies, which are cross linked by shears at 336/82 ENE.

The hanging wall ore body is hosted in highly deformed dolostone and quartzite units ~150 m east of the main ore zone and extends for ~1 km along strike, dipping east. The body is discontinuous in places and is not as clearly structurally controlled as the main zones.

5. Ore mineralisation

Ore styles and textures

Gounkoto features a wide variety of ore textures (Figure 3). These include 1) shear-hosted sulphide stringers; 2) hydrothermal breccias; 3) disseminated sulphides; and 4) hydrothermal veining. Sulphide stringers comprise bands of fractured and deformed pyrite and associated trace phases within chloritic shears (Figure 3A). These overprint chloritised or albitised wall rock, as well as the hanging wall dolostone package and are associated with high grades up to 89 g/t Au. Breccia hosted mineralisation at Gounkoto typically affects strongly albitised rocks, which makes up the clasts, while the matrix consists of dolomite–pyrite–chlorite±magnetite±tourmaline. Breccia styles vary from hydrothermal jigsaw breccias (Figure 3B) to tectonised breccias (Figure 3C and D) in which clasts have undergone elongation, rounding and size reduction during deformation. Less deformed breccias regularly show low grades (<1 g/t Au), whereas more deformed breccias host up to 112 g/t Au (more typically ~20-50 g/t Au). Sulphides also occur as disseminations in altered wall rock (Figure 3E). The volume of disseminated sulphides is variable, but can reach >50 % of the total rock volume; this is generally proportional to ore grade. Auriferous veining at Gounkoto consists of quartz-carbonate-pyrite-chlorite veins. These are typically located several 10s of meters outside the main ore zone, however they are also present in some parts of the Jog Zone, where they have commonly been boudinaged during ongoing deformation. Auriferous vein sets carry grades up to ~70 g/t Au where associated with disseminated ores, but are typically lower grade where observed outside the

main lodes (average ~1.7 g/t Au). Late barren veins cross cut all other ore textures at the Gounkoto deposit. These are typically undeformed 1-2 cm thick carbonate ± quartz veins with a milky appearance (Figure 3B).

Ore mineralogy

The paragenesis of the ore and alteration assemblages at Gounkoto is summarised in Figure 4 and mineral chemistry is given in Table 1 and Table 2. Pyrite is the dominant ore phase at Gounkoto, accounting for ~99 % of the sulphide phases present and ~95 % of ore phases (including magnetite). Auriferous pyrite typically shows two morphologies: highly fractured and rounded pyrites are interpreted to have formed prior to a phase of intense brittle-ductile deformation (Figure 5A). Grain size is variable, but generally <500 µm. Auriferous pyrite is also euhedral to subhedral where present in areas of less intense deformation (Figure 5B and C). Both morphologies are commonly surrounded by anhedral, vuggy and fine-grained (typically <300 µm) pyrite, containing abundant gangue inclusions (Figure 5B and C). This vuggy pyrite is typically associated with low grades (<5 g/t Au). Arsenian pyrite is common at Gounkoto, with As content between 0.1 and 1.9 wt. % (mean of 0.9 wt. %). In addition pyrite at Gounkoto commonly contains Ni content between 0.2 and 7.8 wt. % (mean of 2.7 wt. %), with concentrations generally higher in the hanging wall ore body (mean of 4.4 wt. % Ni) than in the main ore body (mean of 0.9 wt. % Ni).

Magnetite can locally comprise up to 15 % of the ore body at Gounkoto (Figure 5D). Early magnetite occurs as <50 µm inclusions in pyrite or in gangue (Figure 5E). The main phase of magnetite mineralization occurs as cm scale annealed masses of 100 to 800 µm anhedral crystals. This replaces pyrite and is intergrown with dolomite and chlorite (Figure 5F). Replacement coincides with brecciation and remobilization of Au.

Accessory ore phases at Gounkoto include arsenopyrite, pyrrhotite, chalcopyrite, scheelite, apatite, monazite, xenotime, gersdorffite, cobaltite and tennantite. Millerite, galena, clausthalite, ullmannite and polydymite are also present; however these are restricted to the hanging wall ore body (Table 1). Arsenopyrite is the most abundant accessory phase, occurring as <100 µm blebby inclusions in pyrite and early barren, anhedral grains in the main ore body (Figure 5G) and as <200 µm, rhombic crystals associated with disseminated auriferous pyrite in the hanging wall (Figure 5H). Using the geothermometer of Sharp et al. (1985) the range of atomic % As in arsenopyrite at Gounkoto (Table 1) corresponds to formation temperatures of between 315 and 350°C.

Native gold at Gounkoto is dominantly associated with pyrite and arsenian pyrite. Gold occurs as occluded grains within pyrite (Figure 6a), free grains within the gangue (Figure 6b and c); remobilised

grains in fractured or brecciated sulphides and along sulphide-gangue grain boundaries (Figure 6C). Gold grain size is typically <30 µm, but remobilised grains are coarser (up to 200 µm). Gold fineness ranges from 980 to 999 in the main ore body, with average values of 957 in the hanging wall (Table 2). Gold telluride and gold-related trace phases at Gounkoto include Au-bearing phases Bi-sylvanite ([Au, Ag, Bi]Te_2), petzite (Ag_3AuTe_2) and calaverite ($AuTe_2$)(Figure 6a) and non-Au-bearing phases altaite (PbTe)(Figure 6D), clausthalite (PbSe), native tellurium and bismuth (Table 2).

6. Alteration

Alteration at Gounkoto is characterized by a number of distinct hydrothermal assemblages. These include: 1) sodic alteration; 2) carbonate alteration; 3) chloritisation; and 4) tourmalinisation (minor) (Figure 4). Albitisation and tourmalinisation have been described in detail at the Gara and Yalea deposits by Lawrence et al (2013a).

Albitisation

Sodic alteration at Gounkoto predates mineralization. Hydrothermal breccias contain clasts of intensely albitised sedimentary rocks (Figure 3B, C and D) and auriferous veining in the Jog Zone of the deposit cross cuts albitised sediment packages. The albitised mineral assemblage comprises <20 – 100 µm albite with interstitial carbonate (<20 to 500 µm; consisting of Fe-Mn bearing dolomite) and accessory haematite (~10 µm), with trace apatite and monazite. Feldspars are altered to near pure albite (typically <0.5 wt. % K_2O and <1wt. % CaO). Albitised lithologies at Gounkoto are relatively brittle and impermeable compared to unaltered sedimentary rocks and chloritic shear zones. In some cases, this competence contrast has apparently worked to enhance the grades in shear zones that form adjacent to boudins of albitised rock. In some sections of the ore body however, albitised rocks become brecciated, with significant mineralization hosted within the cement.

Tourmalinisation

Tourmalinisation at Gounkoto is not widespread. Minor tourmalinite units (metaquartzwacke with tourmalinized phyllic matrix) are present, but are highly subordinate and weakly mineralized (<0.5 g/t Au). Syn-mineralisation tourmaline is also present as a minor gangue mineral in hydrothermal-tectonic breccias and shear hosted mineralized zones.

Chloritisation

Ductile chloritic shears are the dominant ore host at Gounkoto (Figure 3A) and comprise well-foliated, undulose aggregates of fine-grained (<150 µm) chlorite crystals (Figure 5A). These shears

host auriferous sulphide phases (+magnetite) and overprint or cross-cut albite alteration. Individual shears are 100 µm to ~1 mm across and make up shear zones 10s of meters across. In parts of the Jog Zone discrete shears give way to pervasive chloritisation of the wall rock. Chlorite is also present as an accessory phase in the selvage of auriferous dolomite-quartz-pyrite veins. Post-ore chlorite at Gounkoto has replaced sulphide and oxide ore minerals. Chlorite mineral compositions at Gounkoto include brunsvigite, pycnochlorite, ripidolite and daphnite. The chlorite geothermometer of Cathelineau (1988), modified by Kranidiotis and Maclean (1987), gave a range of temperatures for syn-mineralisation chlorites between 235 and 364 °C (mean of 293 °C; *n*=38). Replacement stage chlorites show slightly broader range between 160 and 333 °C (mean of 301 °C; *n*=10).

Carbonate overprinting

In albitised units cross cut by mineralized chloritic shears and carbonate-pyrite veinlets, carbonate content of the rock can increase dramatically (up to 60 volume %). This takes the form of pervasive disseminated carbonate (which bleaches the rock; Figure 3D) and/or halos of Fe-rich carbonate surround veins and shears, producing deep red coloured alteration halos. This indicates multiple phases of carbonate alteration; with pervasive overprint of the albite alteration followed by more localized halos. In some lower grade parts of the deposit very coarse (up to 4 mm) euhedral dolomite crystals are disseminated throughout variably albitised host rock.

7. Fluid Inclusions

Petrography and timing of fluid inclusions

The four primary types of fluid inclusion reported by Lawrence et al., (2013b) are recognised in this study. These are: Type-I) $CO_2 \pm N_2 \pm CH_4$ inclusions (Figure 7a); type-II) H_2O-NaCl inclusions (Figure 7b); type-III) H_2O-CO_2-NaCl $\pm N_2 \pm CH_4$ inclusions (Figure 7c) and; type-IV) hypersaline, multiphase H_2O-CO_2-NaCl-$FeCl_2 \pm CH_4 \pm N_2$ inclusions (Figure 7d). Type-I inclusions are dominant at Gounkoto and account for 69 % of the inclusions measured, while type-II account for 7% and type-III for 22 %. Type-IV are rare, with 4 inclusions analysed (2 %).

Type-I CO_2-rich inclusions are mono- (LCO_2) (dominant) or bi-phase ($LCO_2 + VCO_2$) at 20°C. They are <5 to 30 µm, rounded to oblate, with rare negative crystal shapes and occur in randomly orientated clusters, often with type-III and rarely type-II inclusions. Type-II aqueous inclusions range in size from <2 µm to ~15 µm, are bi-phase at 20°C ($LH_2O + VH_2O$), show rounded or rare negative crystal shapes and occur as isolated inclusions or in small clusters with or without inclusion types-I and -III. Type-III immiscible H_2O-CO_2 inclusions show a broad range of modal proportions between 20 and 85 vol. % CO_2. At 20°C, these inclusions are two- ($LH_2O + LCO_2$) and, less commonly, three-phase ($LH_2O + LCO_2$

+ VCO_2). They are oblate to well-rounded, 5-20 μm in diameter and occur as individual inclusions or in discrete clusters with type-I and rarely type-II inclusions. Type-IV multiphase solid aqueous-rich inclusions are present in only one sample at Gounkoto. Type-IV inclusions contain mono- or bi-phase (at 20 °C) CO_2 and one to three visible daughter minerals. Inclusions are <5 to 10 μm, rounded and occur with inclusions of type-I and -III.

Microthermometry

Microthermometric data from Gounkoto is summarised in Table 3 and calculated bulk composition and density data is given in Table 4.

Type-I inclusions have a range in CO_2 melting temperatures (T_mCO_2) from -60.9 to -57.7 °C (mean of -58.7 °C) (Figure 8A). Depression of the CO_2 eutectic implies the presence of variable concentrations of N_2 and/or CH_4. Laser Raman analysis has confirmed the presence of 1.8 to 21.5 molar % N_2 and 0.6 to 1.1 molar % CH_4. The homogenisation temperature (T_hCO_2) of type-I inclusions ranges from -5.6 to 30.6 °C (mean of 20.3 °C) (Figure 8B). Inclusions predominantly homogenised into the liquid phase, with 3.2 % of inclusions homogenising to vapour and 4.7 % showing critical behaviour. Calculated fluid density ranges from 0.414 to 0.933 $g \cdot cm^{-3}$ (mean of 0.732 $g \cdot cm^{-3}$) (Figure 8C).

Type-II inclusions at Gounkoto exhibit final ice melting temperatures ($T_m$ice) from -4.9 to -0.2 °C (mean of -2.7 °C), with salinities between 0.35 and 7.7 wt. % NaCl equivalent (mean of 4.3 wt. %). Final homogenisation temperatures (T_hH_2O) vary considerably, from as low as 146 °C (possibly leaked) up to 365 °C (mean of 233 °C). The majority of T_hH_2O values are above 200 °C (*n*=8). Calculated fluid density ranges from 0.66 to 0.97 $g \cdot cm^{-3}$ (mean of 0.848 $g \cdot cm^{-3}$)(Figure 8D).

T_mCO_2 in type-III inclusions ranges from -62.3 °C to -58.1 °C (mean of -58.6 °C), and T_hCO_2 ranges from -14.4 to 29.7 °C (mean of 18.2 °C; homogenisation to liquid)(Figure 8A and B). Clathrate melting temperatures ($T_m$cl) from -12.9 to 9.7 °C (mean of 5.9 °C) indicate salinities between 0.6 and 26.3 wt. % NaCl equivalent (mean of 6.4 wt. %) (Figure 8F). The majority of type-III inclusions have a $T_m$cl range between 4.4 and 9.7 °C (0.6 to 9.95 wt. % NaCl). However, type-III inclusions in one sample exhibit $T_m$cl from -12.9 to 7.9 °C (4.15 to 26.3 wt. % NaCl equivalent). Total homogenisation temperature (T_h tot) was only measured for 25 (~70 %) of type-III inclusions analysed (Figure 8E); the rest either decrepitated (T_d) or showed no identifiable change. T_d values range from 200 to 300 °C (mean of 257 °C) and are treated as minimum estimates of homogenisation temperatures. T_h tot values range from 240 to 370 °C (mean of 322 °C). Bulk densities (ρ_{tot}) for the variable salinity

population range from 0.863 to 1.056g·cm^{-3} (mean of 0.955g·cm^{-3}), while the majority range from 0.694 to 1.044g·cm^{-3}.

Type-IV inclusions are extremely rare at Gounkoto (*n*=4) and microthermometric data are thus incomplete. T_mCO_2 and T_hCO_2 of the gaseous phase ranged from -60 to -57.3 and 1.7 to 15.7 °C, respectively. Reliable salinity data is scarce; one T_sNaCl temperature at 343 °C indicates a salinity of 41.2 wt. % NaCl equivalent. Salinity estimates calculated from volumetric proportions give values of 36.8 and 38.6 wt. % NaCl equivalent; all salinity data are within the range for type-IV inclusions reported by Lawrence et al. (2013b; 36.9 to 44.5 wt. % NaCl equivalents). Two homogenisation temperatures were observed at 445 and 460 °C. Calculated ρ_{tot} is between 1.13 and 1.27g·cm^{-3}.

8. Stable isotopes

Stable isotope data from Gounkoto are summarised in Table 5. Auriferous pyrite at Gounkoto shows a δ^{34}S range from 5.8 to 12.8 ‰ (n=18; mean of 8.6 ± 2 ‰). Au-bearing arsenopyrite yielded a single δ^{34}S value of 8.8 ‰ (Figure 9A). No diagenetic sulphides have been observed in the wall rocks at Gounkoto, therefore in order to compare against δ^{34}S values of auriferous pyrite, diagenetic pyrite samples were collected from barren dolostone units in the Kofi Series at Baqata, Kolya, Gara and Yalea (Figure 1b); these show a range of values from 6.4 to 25.1 ‰ (n=4; includes data from Lawrence et al., 2013b). Quartz from auriferous veining yielded δ^{18}O values between 12.9 and 17.4 ‰ (n=6; mean of 16 ± 1.5 ‰). δ^{18}O values from dolomite in Au-bearing veins ranges from 14.7 to 20.5 ‰ (n=8; mean of 17.3 ± 2.2 ‰) (Figure 9B). Dolomite from barren carbonate veins has similar values at 18.2 ‰ (n=2). Two δ^{18}O values were also obtained from hematite and one from magnetite in the Gounkoto ore body, these were -1.4 (n=2) and 4.2 ‰, respectively. Calculated $\delta^{18}O_{fluid}$ values range from 7.3 to 15.3 ‰, calculated from quartz, dolomite and magnetite using the equations of Matsuhisa et al. (1979), Zheng et al. (1999) and Zheng and Simon (1991). Auriferous vein carbonates have δ^{13}C values between -13.6 and -6.3 ‰ (n=8; mean of -9.1 ± 2.2 ‰). Carbonate minerals from late barren veining and wall rock dolostones gave values between -3.1 and -0.5 ‰ (n=3; mean of -2 ‰) (Figure 9C). The two equilibrium temperatures were calculated from quartz-dolomite mineral pairs at 344 and 346 °C using the equations of Zheng et al. (1999).

9. Discussion

Fluid immiscibility at Gounkoto

Lawrence et al., (2013b) interpreted the fluid inclusion assemblages at the Yalea deposit to represent immiscible fluids formed through unmixing of a common parent fluid. Similar inclusion assemblages are observed at Gounkoto and show broadly similar behaviour. Type-I, -II and -III

inclusions at Gounkoto indicate that some level of fluid immiscibility was reached during entrapment. Ramboz et al., (1982) report criteria for identifying fluid immiscibility. These state that pairs of liquid- and vapour-rich inclusions must: 1) demonstrate simultaneous trapping; 2) homogenize in a comparable temperature range via opposite modes of homogenisation; and 3) decrepitate in a comparable temperature range if they are similar in size and shape.

Type-I and type-II inclusions at Gounkoto occur in the same assemblages, thus satisfying (1). Type-III inclusions show behaviour which supports criteria 2 in that those inclusions with >50 vol. % CO_2 tend to homogenise into the CO_2 phase and vice versa within the same temperature range. The third criterion is difficult to assess, as only limited decrepitation data were recorded (n=5). Nevertheless, compositional similarities between inclusion types imply a common origin. Type-II and –III inclusions exhibit similar salinities (Figure 8F). $TmCO_2$ and $ThCO_2$ are comparable in type-I and -III inclusions indicating similar compositions and densities (Figure 8A and B). Lastly, type-III inclusions exhibit higher Th than type-II, a phenomenon commonly associated with fluid immiscibility (Roedder, 1984). The variable phase proportions (XCO_2 from 0.06 to 0.55) in type-III inclusions suggest that they represent heterogeneous trapping of the two end member fluids (Diamond, 1990; Yao et al., 2001; Lawrence et al., 2013b).

As with many Birimian deposits, Gounkoto features a higher proportion of CO_2-rich inclusions compared to aqueous and aqueous-carbonic inclusions (Schwartz et al., 1992; Hammond and Shimazaki, 1994; Klemd and Hirdes, 1997; Klemd et al., 1997; Willie and Klemd, 2004; Lawrence et al., 2013b); though this is not always the case (Treloar et al., 2014). This is not an observation normally associated with fluid immiscibility, but could be explained by: 1) water loss along migrating grain boundaries (Hollister, 1990) or through diffusion (Bakker, 2009); 2) phase separation at the crystal boundary due to the different wetting properties of H_2O and CO_2 (Holness, 1993; Johnson and Hollister, 1995); 3) consumption of H_2O via thermal degradation of ethane (Gaboury, 2013). Water leakage can be dismissed, as the ρCO_2 in type-I and –III inclusions is comparable; water leakage would lower the density of the remaining CO_2 (Yao and Robb, 2000). Crystal boundary phase separation cannot be ruled out and may have enhanced the immiscibility of the fluid during entrapment, resulting in the pure end member phases described in type-I and -II inclusions. Gaboury (2013) reported carbonaceous shale sourced C_2H_6 in fluid inclusions from the Mana District in Burkina Faso and observed that the thermal degradation of C_2H_6 under hydrothermal conditions would consume H_2O and enrich the fluid in CO_2, which could generate CO_2-rich assemblages such as at Gounkoto.

P-T conditions of fluid trapping

The P-T trapping conditions at Gounkoto were calculated using intersecting isochores of type-I and type-II fluid inclusions (constructed using the software package FLUIDS) (Bakker, 2003)(Figure 10), in combination with arsenopyrite (315 to 350 °C) and quartz-dolomite isotope equilibria temperatures (344 °C and 346 °C). P-T conditions are estimated at 1.1 to 1.7 kbar (depth of 4.1 to 6.2 km) and 315 to 356 °C; the mean isochores for type-I and -II inclusions intersect at 1.4 kbar and 340 °C.

Fluid mixing at Gounkoto

Lawrence et al. (2013b) reported partial mixing between a hypersaline fluid and a dilute aqueous-carbonic fluid at the Gara deposit. Type-IV inclusions co-occurring with type-III inclusions with uncharacteristically variable salinities suggest a similar process at Gounkoto, with the brine enhancing the salinity of type-III inclusions (Figure 11). This mixing occurred in discrete parts of the Gounkoto deposit. Type IV inclusions are only observed in the Jog Zone, implying a structural control on fluid interaction. It is conceivable that fluids could remain segregated due to pooling in between failure events. This may imply that the hypersaline fluid is being introduced along brittle structures, which failed periodically and introduced pulses of the fluid into the system.

Causes of fluid immiscibility and effect of fluid mixing

Phase separation via effervescence occurs in H_2O-CO_2-NaCl fluids when the immiscibility field expands to higher temperatures in response to lower pressures due to a reduction in the solubility of CO_2 and other volatiles (Brown and Lamb, 1989). This can be demonstrated at Gounkoto through 1): the wide range in ρCO_2 of type-I inclusions suggesting pressure fluctuations such as those associated with fault valve systems (Sibson, 1989; Cox et al., 2005); and 2) lower T_h values in type-II inclusions (~232 °C) compared to type-III (~322 °C), suggesting the removal of CO_2 from solution which reduces the pressure, and therefore homogenisation temperature, of the remaining aqueous phase (Robert and Kelly, 1987). An increase in salinity of the aqueous-carbonic fluid would further decrease the solubility of CO_2 (Zhang and Frantz, 1992; Diamond, 2001). Thus, mixing with the hypersaline fluid would have enhanced phase separation in the aqueous-carbonic fluid (Anderson et al., 1992).

Gold precipitation at Gounkoto

In an aqueous-carbonic fluid at around 1.4 Kbar and 340 °C, Au is most likely to be transported as thiosulphide complexes ($Au(HS)^o$ or $Au(HS)_2^-$) (Ridley et al., 1996; Williams-Jones et al., 2009). It is unclear if the hypersaline fluid is auriferous; it should be noted that large Au deposits such as Yalea have formed in its absence (Lawrence et al., 2013b). This implies that the hypersaline fluid at Gounkoto may be primarily important as a trap and not a significant Au carrier. This is further

supported by the instability of Au-Chloride complexes at low fO_2 and near neutral pH conditions (Williams-Jones and Migdisov, 2014). Fluid inclusion assemblages, ore textures and paragenetic relationships at Gounkoto indicate that Au precipitation was most likely caused by a combination of: (1) phase separation; (2) wall rock sulphidation; and (3) reduction of the ore fluid (Ridley et al., 1996). These processes would destabilise Au thiosulphide complexes, leading to Au precipitation. Wall rock sulphidation at Gounkoto was likely dominant in areas of the deposit featuring disseminated sulphides. Whereas brecciated and the subordinate veined ore textures are likely more closely linked to phase separation, where brittle failure would have resulted in rapid fluid pressure fluctuations. Further, interaction with reduced organic carbon in the hanging wall dolostone is supported by relatively light $\delta^{13}C$ values exhibited by carbonate minerals in auriferous veining (-13.6 to -9 ‰), a similar phenomenon was observed by Lawrence et al., (2013b) at the Yalea deposit.

Volatile and metal sources at Gounkoto

The low salinity (<5 wt. % NaCl equiv.), moderate temperature CO_2-rich, H_2O-CO_2-NaCl fluid at Gounkoto closely resembles the 'model fluid' for orogenic gold deposits (c.f. Ridley and Diamond, 2000; Garofalo et al., 2014). Many regard these fluids to be derived from prograde metamorphic devolatilisation reactions (McCuaig and Kerrich, 1998; Tomkins 2010; Phillips and Powell, 2010; Yardley and Cleverly, 2013). Stable isotope analysis of O, C and S from ore and vein phases at Gounkoto supports this interpretation. Calculated $\delta^{18}O_{fluid}$ values at Gounkoto plot dominantly in the metamorphic water field of Ohmoto and Goldhaber (1997). Positive $\delta^{34}S$ values in auriferous pyrite (5.8 to 12.8 ‰) sit within the range for Kofi Series diagenetic pyrite (6.4 to 25.1 ‰), suggesting derivation from desulphidation of diagenetic pyrite (Pitcairn et al., 2006; Phillips and Powell, 2010). Similarly, $\delta^{13}C$ data (-13.6 to -6.3 ‰) suggest that carbon in auriferous veins is derived from a mixed sourced, comprising: 1) dissolution of carbonate minerals within the Kofi Series (-2 ‰) and; 2) oxidation of graphite derived from organic material hosted in dolostone units (Palaeoproterozoic $\delta^{13}C_{org} \approx$ -24±6 ‰) (Schidlowski, 1983). The hypersaline fluid inclusions observed at Gara, Yalea North (Lawrence et al., 2013b) and Gounkoto are uncommon in the wider Birimian. Lawrence et al., (2013b) discussed the possibility of evaporite dissolution in their generation, but ultimately interpreted the fluids to be of magmatic origin. This was based upon the apparent higher temperature and the metaliferous composition of the brines ($FeCl_2$-rich). However, the lack of a magmatic signature in the stable isotope dataset at Gounkoto forces us to reconsider this position. The presence of heavy $\delta^{34}S$ values (19.7 and 25.1 ‰) in Kofi Series diagenetic pyritemay support the former presence of evaporite units in the Kofi. Pyrite formed through the reduction of evaporitic sulphate minerals (e,g. anhydrite) has been shown to inherit diagnostically high $\delta^{34}S$ values (c.f.

Monteiro et al., 2008). This suggests that the dissolution of evaporite units within the Kofi Series may indeed a viable source for these brines. Nevertheless, the high homogenization temperatures recorded for the brine (up to 445 °C) cannot be ignored and therefore a magmatic source cannot be wholly ruled out. We consider that the apparently subordinate nature of the hypersaline fluid could result in the dilution of any magmatic isotopic signature to the point of being undetectable.

Conclusions

The Gounkoto deposit formed at P-T conditions of approximately 1.4 kbar and 340 °C and features mineralogical and fluid chemical characteristics in common with both Gara- and Yalea-style mineralisation as described by Lawrence et al., (2013a and b). These include sodic and B-metasomatism, As-rich ore assemblages and Ni-Co substitution in pyrite. The ore body also features some distinct characteristics, including the presence of significant quantities of magnetite, sellenide trace minerals and telluride ore phases.

The end member fluids identified by Lawrence et al., (2013b) at Gara and Yalea are also identified at Gounkoto: (1) a moderate temperature (315-340 °C), low salinity (<10 wt. % NaCl equiv.), low density (≤1 gcm^{-3}), H_2O-CO_2-NaCl-H_2S±N_2-CH_4 fluid; (2) a high temperature (up to 445 °), hypersaline (~40 wt. % NaCl equiv.), high density (~1.3 gcm^{-3}), H_2O-CO_2-NaCl±$FeCl_2$ fluid. Partial mixing of these fluids within the Jog Zone at Gounkoto enhanced phase separation in the aqueous-carbonic fluid and acted as a precipitation mechanism for Au. These findings demonstrate the widespread, if heterogeneously distributed, nature of fluid mixing as an ore forming process in the Loulo-Gounkoto complex, operating over at least a 30 km strike length of the shear zone.

Stable isotope analyses of ore components at Gounkoto indicate a dominant metamorphic source for H_2O, H_2S and CO_2, and by extension Au. It thus can be reasoned that both the aqueo-carbonic and the hypersaline fluid at Gounkoto are of metamorphic origin and that the high levels of salinity in the brine are likely derived from evaporite dissolution.

Acknowledgements

The data presented in this paper forms part of a Ph.D. project by J. S. Lambert-Smith, for which financial and scientific support by Randgold Resources Ltd and Kingston University is gratefully received. Isotope analyses were carried out through a NERC Facilities Grant (IP-1252-0511) to P. J. Treloar. A. J. Boyce is funded by NERC support to the Isotope Community Support Facility at SUERC.

References

Abouchami, W., Boher, M., Michard, A. and Albarede, F., 1990. A major 2.1 Ga event of mafic magmatism in West Africa: an early stage of crustal accretion. Journal of Geophysical Research, 95: 17605-17629.

Allibone, A., Teasdale, J., Cameron, G., Etheridge, M., Uttley, P., Soboh, A., Appiah-Kubi, J., Adanu, A., Arthur, R., Mamphey, J., Odoom, B., Zuta, J., Tsikata, A., Pataye, F. and Famiyeh, S., 2002a. Timing and structural controls on gold mineralisation at the Bogoso gold mine, Ghana, West Africa. *Economic Geology*, **97**, 949-969.

Anderson, M.R., Rankin, A.H. and Spiro, B., 1992. Fluid mixing in the generation of mesothermal gold mineralisation in the Transvaal Sequence, Transvaal, South Africa. European *Journal of Mineralogy*, **4**, 933-948.

Archer, D. G., 1992. Thermodynamic Properties of the NaCl+ H_2O System. II. Thermodynamic Properties of NaCl (aq), NaCl·$2H_2$ (cr), and Phase Equilibria. *Journal of Physical and Chemical Reference Data*, **21**, 793.

Bakker R. J., 1999. Adaption of Bowers and Helgeson (1983) equation of state to isochore and fugacity coefficient calculation in the H_2O-CO_2-CH_4-N_2-NaCl fluid system. *Chemical Geology*, **154**, 225-236.

Bakker R. J. 2009. Reequilibration of fluid inclusions: Bulk-diffusion. *Lithos*, **112**, 277-288.

Bakker R. J., 2003. Package FLUIDS 1. Computer programs for analysis of fluid inclusion data and for modelling bulk fluid properties. *Chemical Geology*, v. **194**, 3-23.

Bowers, T.S. and Helgeson, H.C., 1983a. Calculations of the thermodynamic and geochemical consequences of non-ideal mixing in the system H_2O-CO_2-NaCl on phase relations in geological systems. Equation of state for H_2O-CO_2-NaCl fluids at high pressures and temperatures. *Geochimica et Cosmochimica Acta*, **47,** 1247-1275.

Bowers, T.S. and Helgeson, H.C., 1983b. Calculations of the thermodynamic consequences of non-ideal mixing in the system H_2O-CO_2-NaCl on phase relations in geological systems. *American Mineralogist*, **68**, 1059-1075.

Brown, P.E. and Lamb, W.M., 1989. P-V-T properties of fluids in the system $H_2O \pm CO_2 \pm$ NaCl: New graphical presentations and implications for fluid inclusion studies. *Geochimica et Cosmochimica Acta*, **53**, 1209-1221.

Burke, E.A.J., 2001. Raman microspectrometry of fluid inclusions. *Lithos*, **55**, 139-158.

Cathelineau, M., 1988. Cation site occupancy in chlorides and illites as a function of temperature. *Clay Minerals*, **23**, 471-485.

Cox, S.F., 2005. Coupling between deformation, fluid pressures and fluid flow in ore-producing hydrothermal systems at depth in the crust. *Economic Geology 100th Anniversary Volume*, 1–35.

Craig, H., 1957. Isotopic standards and isotopic correction factors for mass spectrometric analysis of carbon dioxide. *Geochimica et Cosmochimica Acta*, **12**, 133-149.

Dabo, M., and Aïfa, T., 2010. Structural styles and tectonic evolution of the Kolia-Boboti sedimentary Basin, Kédougou-Kéniéba inlier, eastern Senegal. *Comptes Rendus Geoscience*, **342**, 796-805.

Dabo, M., and Aïfa, T., 2011. Late Eburnean deformation in the Kolia-Boboti sedimentary basin, Kedougou-Kenieba Inlier, Senegal. *Journal of African Earth Sciences*, **60**, 106-116.

Diamond, L.W., 1990. Fluid inclusion evidence for P-V-T-X evolution of hydrothermal solutions in Late-Alpine gold-quartz veins at Brusson, Val D'Ayas, Northwest Italian Alps. *American Journal of Science*, **290**, 912-958.

Diamond, L. W., 2001. Review of the systematics of CO_2–H_2O fluid inclusions. *Lithos*, **55**, 69-99.

Duan, Z., Møller, N., and Weare, J. H., 1996. A general equation of state for supercritical fluid mixtures and molecular dynamics simulation of mixture PVTX properties. *Geochimica et Cosmochimica Acta*, **60**, 1209-1216.

Duan, Z., Møller, N., and Weare, J. H., 1992. An equation of state for the CH_4-CO_2-H_2O system: I. Pure systems from 0 to 1000°C and 0 to 8000 bar.*Geochimica et Cosmochimica Acta*, **56**, 2605-2617.

Feybesse, J. and Milési, J.P., 1994. The Archaean/Proterozoic contact zone in West Africa: a mountain belt of decollement thrusting and folding on a continental margin related to 2.1 Ga convergence of Archean cratons? *Precambrian Research*, **69**, 199-227.

Feybesse, J., Billa, M., Guerrot, C., Duguey, E., Lescuyer, J., Milési, J.P. and Bouchot, V., 2006. The Palaeoproterozoic Ghanaian province: Geodynamic model and ore controls, including regional stress modelling. *Precambrian Research*, **149**, 149-196.

Gaboury, D., 2013, Does gold in orogenic deposits come from pyrite in deeply buried carbon-rich sediments? Insight from volatiles in fluid inclusions: *Geology*, **41**, 1207–1210.

Garofalo, P.S., Fricker, M.B., Günther, D., Bersani, D., and Lottici, P.P., 2014. *Physical-chemical properties and metal budget of Au-transporting hydrothermal fluids in orogenic deposits*. In Garofalo, P. S. and Ridley, J. R. (eds.) *Gold-Transporting Hydrothermal Fluids in the Earth's Crust*. Geological Society, London, Special Publications, **402**, 71-102.

Groves, D.I., Goldfarb, R.J., Gebre-Mariam, M., Hagemann, S.G. and Robert, F., 1998. Orogenic gold deposits: A proposed classification in the context of their crustal distribution and relationship to other gold deposit types. *Ore Geology Reviews*, **13**, 7-27.

Hammond, N.Q. and Shimazaki, H., 1994. Geology and geochemical aspects of ore formation at the Prestea mesothermal vein gold deposit in the Birimian system of Ghana. *International Geology Reviews*, **36**, 15-31.

Hirdes, W. and Davis, D.W., 2002. U-Pb Geochronology of Palaeoproterozoic rocks in the southern part of the Kédougou-Kéniéba inlier, Senegal, West Africa: evidence for diachronous accretionary development of the Eburnean Province. *Precambrian Research*, **118**, 83-99.

Hollister, L.S., 1990. Enrichment of CO_2 in fluid inclusions in quartz by removal of H_2O during crystal-plastic deformation. *Journal of Geology*, **12**, 895-901.

Holness, M.B., 1993. Temperature and pressure dependence of quartz-aqueous fluid dihedral angles: the control of adsorbed H_2O on the permeability of quartzites. *Earth and Planetary Science Letters*, **117**, 363-377.

Johnson, E.L., Hollister, L.S., 1995. Syndeformational fluid trapping in quartz: determining the pressure–temperature conditions of deformation from fluid inclusions and the formation of pure CO_2 fluid inclusions during grain-boundary migration. *Journal of Metamorphic Geology*, **13**, 239–249.

Klemd, R. and Hirdes, W., 1997. Origin of an unusual fluid composition in Early Proterozoic palaeoplacer and lode-gold deposits in Birimian greenstone terranes of West Africa. South *African Journal of Geology*, **100**, 405-414.

Klemd, R., Oberthür, T. and Ouedrago, A., 1997. Gold-telluride mineralisation in the Birimian at Diabatou, Burkina Faso. *Journal of African Earth Sciences*, **24**, 227-239.

Kranidiotis, P. and MacLean, W.H., 1987. Systematics of chloride alteration at the Phelps Dodge massive sulphide deposit, Matagami, Quebec. *Economic Geology*, **82**, 1898-1911.

Lawrence, D.M., Treloar P.J., Rankin, A.H., Harbidge, P., and Holliday, J., 2013a. The Geology and Mineralogy of the Loulo Mining District, Mali, West Africa: Evidence for Two Distinct Styles of Orogenic Gold Mineralization, *Economic Geology*, **108**, 199-227.

Lawrence, D.M., Treloar, P.J., Rankin, A.H., Boyce, A., and Harbidge, P., 2013b. A fluid inclusion and stable isotope study at the Loulo mining district, Mali, West Africa: Implications for multifluid sources in the generation of orogenic gold deposits: *Economic Geology*, **108**, 229–257.

Lecumberri-Sanchez, P., Steele-MacInnis, M., and Bodnar, R. J., 2012. A numerical model to estimate trapping conditions of fluid inclusions that homogenize by halite disappearance. *Geochimica et Cosmochimica Acta*, **92**, 14-22.

Ledru, P., Pons, J., Milesi, J. P., Feybesse, J. L. and Johan, V., 1991. Transcurrent tectonics and polycyclic evolution in the lower Proterozoic of Senegal-Mali, *Precambrian Research*, **50**, 337-354.

Matsuhisa, Y., Goldsmith, J.R. and Clayton, R.N., 1979. Oxygen isotopic fractionation in the system quartz-albite-anothite-water. *Geochimica et Cosmochimica Acta*, **43**, 1131-1140.

McCuaig, T.C. and Kerrich, R., 1998. P-T-t deformation-fluid-characteristics of lode gold deposits: Evidence from alteration systematics. *Ore Geology Reviews*, **12**, 381-454.

Milési, J.P., Ledru, P., Feybesse, J., Dommanget, A. and Marcoux, E., 1992. Early Proterozoic ore deposits and tectonics of the Birimian orogenic belt, West Africa. *Precambrian Research*, **58**, 305-344.

Monteiro, L. V., Xavier, R. P., De Carvalho, E. R., Hitzman, M. W., Johnson, C. A., De Souza Filho, C. R., and Torresi, I., 2008. Spatial and temporal zoning of hydrothermal alteration and mineralization in the Sossego iron oxide–copper–gold deposit, Carajás Mineral Province, Brazil: Paragenesis and stable isotope constraints. *Mineralium Deposita*, **43**, 129-159.

Oberthür, T., Vetter, U., Davis, D.W. and Amanor, J.A., 1998. Age constraints on gold mineralisation and Palaeoproterozoic crustal evolution in the Ashanti belt of southern Ghana. *Precambrian Research*, **89**, 129-143.

Ohmoto, H. and Goldhaber, M.B., 1997. Sulphur and carbon isotopes. In: *Barnes, H.I. (Editor), Geochemistry of hydrothermal ore deposits*. 3rd Edition. John Willey and Sons, New York, 517-612.

Phillips, G. N., and Powell, R., 2010. Formation of gold deposits: a metamorphic devolatilization model. *Journal of Metamorphic Geology*, **28**, 689-718.

Pitcairn, I.K., Teagle, D.A., Craw, G.R., Olivo, G.R., Kerrich, R. and Brewer, T.S., 2006. Sources of metals and fluids in orogenic gold deposits: Insights from the Otago and Alpine Schists, New Zealand. *Economic Geology*, **101**, 1525-1546.

Ramboz, C., Pichavant, M. and Weisbrod, A., 1982. Fluid immiscibility in natural processes: use and misuse of fluid inclusion data. II. Interpretation of fluid inclusion data in terms of immiscibility. *Chemical Geology*, **37**, 29-48.

Ridley, J.R. and Diamond, L.W., 2000. Fluid chemistry of orogenic lode gold deposits and implications for genetic models. *Reviews in Economic Geology*, **13**, 141-162.

Ridley, J., Mikucki, E. J., and Groves, D. I., 1996. Archean lode-gold deposits: fluid flow and chemical evolution in vertically extensive hydrothermal systems. *Ore Geology Reviews*, **10**, 279-293.

Robert, F. and Kelly, W.C., 1987. Ore-forming fluids in Archaean gold-bearing quartz veins at the Sigma Mine, Abitibi greenstone belt, Quebec, Canada. *Economic Geology*, **82**, 1464-1482.

Robinson, B.W. and Kusakabe, M., 1975. Quantitative preparation of SiO_2 for $^{34}S/^{32}S$ analysis from sulphides by combustion with cuprous oxide. *Analytical Chemistry*, **47**, 1179-1181.

Roedder, E., 1984. Fluid inclusions. *Reviews in Mineralogy, Mineralogical Society of America*, **12**, 646.

Schidlowski, M., Hayes, J.M. and Kaplan, I.R., 1983. Isotopic inferences of ancient biochemistries: carbon, sulphur, hydrogen and nitrogen. In: *Schopf, J.W. (Editor), Earth's earliest biosphere: it's origin and evolution*. Princeton University Press, New York, 149-186.

Schwartz, M.O., Oberthür, T., Amanor, J. and Gyapong, E.A., 1992. Fluid inclusion re-equilibration and P-T-x constraints on fluid evolution in the Ashanti gold deposit, Ghana. *European journal of mineralogy*, **4**, 1017-1034.

Sharp, Z.D., 1990. A laser-based microanalytical method for the in situ determination of oxygen isotope ratios in silicates and oxides. *Geochimica et Cosmochimica Acta*, **54**, 1353-1357.

Sharp, Z.D., Essene, E.J. and Kelly, W.C., 1985. A re-examination of the arsenopyrite geothermometer: pressure consideration and applications to natural assemblages. *Journal of the Mineralogical Association of Canada*, **23**, 517-534.

Tomkins, A. G., 2010. Windows of metamorphic sulfur liberation in the crust: Implications for gold deposit genesis. *Geochimica et Cosmochimica Acta*, **74**, 3246-3259.

Treloar, P. J., Lawrence, D. M., Senghor, D., Boyce, A., and Harbidge, P. 2015. The Massawa gold deposit, Eastern Senegal, West Africa: an orogenic gold deposit sourced from magmatically derived fluids?. *Geological Society, London, Special Publications*, **393**, 135-160.

Williams-Jones, A.E. and Migdisov, A.A., 2014. Experimental constraints on the transport and deposition of metals in ore-forming hydrothermal systems, in: K.D. Kelley, C.G. Howard (Eds.), Building Exploration Capability for the 21st Century, Society of Economic Geologists, 18, 77–95.

Williams-Jones, A.E., Bowell, R.J. and Migdisov, A.A., 2009. Gold in solution. *Elements*, **5**, 281-287.

Willie, S.E. and Klemd, R., 2004. Fluid inclusion studies of the Abawso gold prospect, near the Ashanti Belt, Ghana. *Mineralium Deposita*, **39**, 31-45.

Yao, Y. and Robb, L.J., 2000. Gold mineralsiation in Palaeoproterozoic granitoids at Obusai, Ashanti region, Ghana: ore geology, geochemistry and fluid characteristics. *South African Journal of Geology*, **103**, 255-278.

Yao, Y., Murphy, P.J. and Robb, L.J., 2001. Fluid characteristics of granitoid-hosted gold deposits in the Birimian terrane of Ghana: A fluid inclusion microthermometric and Raman spectroscopic study. *Economic Geology*, **96**, 1611-1643.

Yardley, B. W., and Cleverley, J. S., 2013. The role of metamorphic fluids in the formation of ore deposits. *Geological Society, London, Special Publications*, **393**, SP393-5.

Zhang, Y.G. and Frantz, J.D., 1987. Determination of homogenisation temperatures and densities of supercritical fluids in the system NaCl-KCl-$CaCl_2$-H_2O using synthetic fluid inclusions. *Chemical Geology*, **64**, 335-350.

Zheng, Y.F., 1999. Oxygen isotope fractionation in carbonate and sulphate minerals. *Geochemical Journal*, **33**, 109-126.

Zheng Y. F. and Simon K., 1991. Oxygen isotope fractionation in hematite and magnetite: A theoretical calculation and application to geothermometry of metamorphic iron-formation. *European Journal of Mineralogy*, **3**, 877-886.

Appendix – Analytical methods

a. Energy-dispersive X-ray spectroscopy

Mineral compositions were determined using an Oxford Instruments X-ACT Energy Dispersive System detector mounted on a Zeiss EVO 50 Scanning Electron Microscope at Kingston University London. The EDS employed an accelerating voltage of 20 kV, a beam current of 1.5 na, and a detector process time of 4. The detection limit for all elements was ~ 0.2 wt %.

b. Microthermometry

Samples of auriferous quartz veins (grades of 0.13 to 27.6 g/t Au) were prepared as doubly-polished ~150 µm wafers. All inclusions analysed were in quartz (*n*=172). Microthermometry was carried out at Kingston University using a Linkam THMSG600 temperature controlled stage with a Nikon Optiphot microscope. The stage was calibrated using Linkam synthetic fluid inclusion standards of pure CO_2 and H_2O. Reproducibility was ±0.2 °C below 30 °C and ±2 °C up to 400 °C.

c. Laser Raman Spectroscopy

Raman analysis was carried out using a Renishaw InVia Raman spectrometer attached to a Leica DM 2500 M microscope. A 500 mW Ar-ion laser (514 nm) was used, with a spot size of ~5 µm. The Raman was calibrated using a CH_4-CO_2 standard. Data reduction was carried out using the WiRE 4 software package, with a running time between 30-60 seconds. Molar fractions were calculated using peak area measurements of the Raman spectra and the formula of (Burke, 2001).

d. Calculations for fluid *PVTx* properties

Calculations of P-V-T-X properties of fluid inclusions, based on the microthermometric data, were made using the software package FLUIDS (Bakker, 2003). The following equations of state were used: Duan et al., (1992; 1996) for carbonic fluid inclusions; Zhang and Frantz (1987) and Archer (1992) for H_2O-NaCl fluid inclusions; and Bowers and Helgeson (1983a, b) and Bakker (1999) for inclusions in the H_2O-CO_2-NaCl system. Salinity was calculated using the equations of Lecumberri-Sanchez et al. (2012), and from estimates of the degree of fill of the inclusions.

e. Stable isotope analysis

Silicate separates were analyzed using a laser fluorination procedure following Sharp (1990). Reproducibility, based on repeat analyses of lab and international standards was better than ±0.3‰ (1σ). Carbonate and sulphide samples were analyzed by standard techniques (Craig, 1957; Robinson and Kusakabe, 1975), with reproducibility of ±0.15‰ for $\delta^{13}C$, ±0.7‰ for $\delta^{18}O$, and ±0.3‰ for $\delta^{34}S$ (1σ). Oxygen, carbon, and sulphur isotopes are reported in standard notation as per mil (‰)

deviations from the Vienna Standard Mean Ocean Water (VSMOW), Vienna PeeDee Belemnite (V-PDB), and Vienna Cañon Diablo Troilite (V-CDT) standards, respectively.

Figure Captions

Figure 1. Geological maps showing (a) the Birimian terranes in West Africa; (b) the geology of the Kédougou-Kéniéba Inlier with key plutons and mines indicated; (c) the geology of the Senegal-Mali Shear Zone around the Loulo-Gounkoto Complex (modified from Lawrence et al., 2013a).

Figure 2. Geological and structural map of the Gounkoto gold deposit.

Figure 3. Photographs of diamond drill core showing: (a) Sulphide stringers associated with chloritic shearing in the jog zone (b) jigsaw style hydrothermal breccia with albitised clasts and carbonate-pyrite cement cross cut by late veining; (c) brecciated albitised sedimentary rock with Fe-rich rims in breccia clasts and ankerite-chlorite-pyrite cement ; (d) brecciated and deformed albitised sedimentary rock with chlorite-carbonate-pyrite veining; and (e) disseminated pyrite ore with interstitial ankerite replacing the host rock.

Figure 4. Summary paragenetic diagram for the Gounkoto deposit.

Figure 5. Reflected light photomicrographs of: (a) deformed pyrite grains hosted in chloritic shears; (b) euhedral auriferous pyrite surrounded by skeletal pyrite in the hanging wall ore body; (c) euhedral inclusion free pyrite surrounded by inclusion-rich anhedral pyrite in low grade ore in the Jog Zone; (d) semi-massive magnetite intergrown with ankerite; (e) haematite corona texture, replacing early magnetite grain in the Wrench Zone; (f) annealed magnetite replacing pyrite. BSE images of (g) blebby arsenopyrite inclusions within pyrite grain; and (h) euhedral arsenopyrite grains in dolostone host rock, note some grains are annealed to pyrite

Figure 6. BSE images of: (a) grains of occluded calaverite and native Au in pyrite; (b) free Au grains hosted in chlorite-ankerite assemblage; (c) free and fracture filling Au associated with pyrite; (d) fractured subhedral pyrite hosting remobilised Au and telluride minerals surrounded by barren skeletal pyrite.

Figure 7. Photomicrographs of: (a) type-I bi-phase CO_2 rich inclusions in an isolated cluster, exhibiting negative crystal shapes; (b) bi-phase low salinity H_2O-NaCl inclusions in early isolated cluster; (c) triple-phase (LH_2O, LCO_2 and VCO_2) type-III H_2O-CO_2-NaCl at 6.6 °C; and (d) type 4 H_2O-NaCl-CO_2-nS inclusion, exhibiting a liquid H_2O phase, liquid CO_2 phase and at least 3 solid phases at room temperature.

Figure 8. Histograms showing: (a) Melting temperature of CO_2 values for type-I and -III inclusions; (b) CO_2 homogenisation values of type-I and -III inclusions; (c) calculated ρCO_2 for type –I and –III inclusions; (d) calculated ρBulk for type-III inclusions; (e) total homogenisation temperatures and decrepitation temperatures for type-III inclusions; and (f) salinity of type-II, -III and –IV inclusions.

Figure 9. Histograms showing: (a) $\delta^{34}S$ data from auriferous and diagenetic sulphides; (b) $\delta^{18}O$ data from auriferous silicate, carbonate and oxide phases; and (c) $\delta^{13}C$ data from auriferous carbonate vein minerals, barren vein carbonate minerals and carbonate from host dolostones sequences. Diagenetic pyrite values at 8 and 10 ‰ are from Lawrence et al. (2013b).

Figure 10. Pressure-temperature-depth plot showing maximum, minimum and mean density isochores for type-I inclusions (solid line) and type-II inclusions (dashed lines) at Gounkoto. Vertical dotted and dashed lines represent the temperature range of arsenopyrite geothermometry and paired oxygen isotope equilibria. The shaded area represents the most likely P-T trapping conditions at the Gounkoto deposit, based on intercepts of arsenopyrite and $\delta^{18}O$ geothermometers.

Figure 11. Plot of salinity versus total homogenisation temperature of type-III and -IV inclusions at Gounkoto showing a weak positive trend, which suggests mixing of the end member brine and aqueous-carbonic fluids.

Tables

Table 1. Representative EDS analyses of sulphide phases in the main ore body and hanging wall ore body at Gounkoto.

					Wt. %						
Mineral	**S**	**Fe**	**Cu**	**As**	**Ni**	**Co**	**Sb**	**Pb**	**Se**	**Total**	**At. % As**
Main ore body											
Arsenopyrite	22.0	35.9	-	41.5	-	-	-	-	-	99.5	-
Arsenopyrite	21.7	35.3	-	42.9	-	-	-	-	-	99.9	30.5
Arsenopyrite	21.2	35.5	-	42.6	-	-	-	-	-	99.3	30.5
Arsenopyrite	22.0	35.9	-	41.5	-	-	-	-	-	99.5	29.4
Arsenopyrite	21.5	36.0	-	41.3	-	-	-	-	-	98.8	29.5
Arsenopyrite	21.6	35.5	-	42.3	-	-	-	-	-	99.5	30.1
Arsenopyrite	22.2	36.2	-	41.7	-	-	-	-	-	100.2	29.3
As-Co-Pyrite	51.4	43.3	-	1.2	-	3.2	-	-	-	99.0	-
As-Pyrite	52.0	46.7	-	1.9	-	-	-	-	-	100.6	-
As-Pyrite	54.1	46.7	-	0.1	-	-	-	-	-	100.9	-
As-Pyrite	52.8	46.5	-	0.9	-	-	-	-	-	100.2	-
As-Pyrite	52.6	46.6	-	0.5	-	-	-	-	-	99.8	-
Chalcopyrite	34.6	30.7	34.7	0.0	-	-	-	-	-	99.9	-
Co-Arsenopyrite	21.4	32.3	-	41.9	-	4.0	-	-	-	99.7	-
Cobaltite	20.7	3.5	-	43.3	-	33.4	-	-	-	100.8	-
Gersdorffite	20.0	11.0	-	43.1	24.4	-	-	-	-	98.6	-
Ni-Pyrite	50.5	45.1	_	2.8	1.2		-	-	-	99.6	-
Ni-Pyrite	50.7	43.9	_	3.3	1.1		-	-	-	98.8	-
Ni-Pyrite	51.0	45.1	_	3.6	1.3		-	-	-	101.1	-
Ni-Pyrite	52.8	45.5	2.7	_	0.4		-	-	-	101.3	-
Ni-Pyrite	52.6	45.2	_	_	1.0		-	-	-	98.8	-
Ni-Pyrite	53.2	43.6	0.8	_	1.3		-	-	-	98.9	-
Pyrite	53.3	47.0	-	-	-	-	-	-	-	100.3	-
Pyrrhotite	38.7	60.9	-	-	-	-	-	-	-	99.6	-
Tennantite	29.2	7.3	43.5	19.5	-	-	-	-	-	99.6	-
Hanging wall ore body											
Arsenopyrite	21.4	35.4	-	42.1	-	-	-	-	-	98.9	30.1
Arsenopyrite	21.8	35.7	-	41.8	-	-	-	-	-	99.3	29.7
Chalcopyrite	35.3	30.9	33.9	-	-	-	-	-	-	100.0	-
Clausthalite	3.3	-	-	-	-	-	-	76.3	20.2	99.9	-
Cobaltite	21.2	5.0	-	42.6	7.3	24.7	-	-	-	100.8	-
Galena	11.3	-	-	-	-	-	-	87.0	2.7	100.9	-
Millerite	35.2	1.3	-	-	63.6	-	-	-	-	100.0	-
Ni-Pyrite	53.0	44.4	-	-	2.8	-	-	-	-	100.2	-
Ni-Pyrite	53.9	41.7	-	-	5.0	-	-	-	-	100.6	-
Ni-Pyrite	53.1	40.3	-	-	7.8	-	-	-	-	101.3	-
Ni-Pyrite	53.6	43.3	-	-	4.4	-	-	-	-	101.3	-
Ni-Pyrite	53.9	41.7	-	-	4.9	-	-	-	-	100.6	-
Ni-Pyrite	53.4	43.9	-	-	3.3	-	-	-	-	100.5	-
Pentlandite	33.3	28.6	-	1.3	35.7	1.4	-	-	-	100.3	-
polydymite	41.7	11.8	-	-	46.1	-	-	-	-	99.6	-
Pyrite	53.3	47.2	-	-	-	-	-	-	-	100.5	-
Pyrrhotite	39.1	61.1	-	-	-	-	-	-	-	100.2	-
Ullmannite	14.7	-	-	-	28.0	-	57.3	-	-	100.0	-

Table 2. Representative EDS analyses of native Au and related trace phases in the main ore body and the hanging wall ore body at Gounkoto.

Mineral Phase	Te	Au	Ag	Pb	Se	Cd	Total
Main ore body							
Altaite	39.52	0.00	0.00	60.05	0.00	0.00	99.57
Au	0.00	99.68	1.05	0.00	0.00	0.00	100.74
Au in Gangue	0.00	99.70	0.53	0.00	0.00	0.00	100.23
Au in Gangue	0.00	100.10	0.00	0.00	0.00	0.00	100.10
Au in Gangue	0.00	98.18	1.78	0.00	0.00	0.00	99.96
Au Occluded	0.00	98.56	0.53	0.00	0.00	0.11	99.20
Au remobilised	0.00	98.02	1.11	0.00	0.00	0.00	99.13
Au remobilised	0.00	98.47	0.96	0.00	0.00	0.00	99.43
Clausthalite	0.00	0.00	0.00	72.24	27.87	0.00	100.12
Tellurium	100.03	0.00	0.00	0.00	0.00	0.00	100.03
Hanging wall ore body							
Au	0.00	95.86	4.22	0.00	0.00	0.00	100.08

Table 3. Summary of microthermometric data from fluid inclusions at Gounkoto

Type	**Tm(CO_2)**	**Tm(Cl)**	**Tm(ice)**	**Th(CO_2)(L)**	**Th(CO_2)(V)**	**Th(CO_2)(C)**	**Ts**	**Th(V)**	**Th(L)**	**Td**
Type-I										
Min	-60.9	-	-	-5.6	25.4	26.0	-	-	-	-
Max	-57.7	-	-	30.6	26.3	27.3	-	-	-	-
Mean	-58.7	-	-	19.8	25.9	26.6	-	-	-	-
N	*63.0*	-	-	*56.0*	*2.0*	*3.0*	-	-	-	-
Type-II										
Min	-	-	-4.9	-	-	-	-	-	146.0	0.7
Max	-	-	-0.2	-	-	-	-	-	364.8	0.9
Mean	-	-	-2.7	-	-	-	-	-	232.5	0.8
N	-	-	*12.0*	-	-	-	-	-	*12.0*	*11.0*
Type-III										
Min	-62.3	-12.9	-	-14.4	-	-	-	270.5	240.0	200.0
Max	-58.1	9.7	-	29.7	-	-	-	369.5	340.3	300.0
Mean	-58.6	5.9	-	18.2	-	-	-	328.1	298.4	256.5
N	*35.0*	*36.0*	-	*36.0*	-	-	-	*20.0*	*5.0*	*5.0*
Type-IV										
1	-58.1	-	-	1.7	-	-	-	-	-	-
2	-59.0	-11.2	-	15.7	-	-	-	-	-	-
3	-60.0	-9.5	-	7.0	-	-	-	-	445.0	-
4	-57.3	-	-		-	-	342.8	-	460.0	-

Table 4. Summary of calculated bulk composition and density data, including compositions derived from laser raman analyses at Gounkoto. χ refers to molar proportions.

				Molecular %			χ		
	Wt. % NaCl equiv.	ρCO_2 (gcm^{-3})	ρTotal (gcm^{-3})	CO_2	N_2	CH_4	H_2O	NaCl	CO_2
Type-I									
Min	-	0.22	-	78.48	0.00	0.00	-	-	1.00
Max	-	0.93	-	99.38	21.52	1.07	-	-	1.00
Mean	-	0.69	-	91.97	7.53	0.50	-	-	1.00
N	-	*60*	-	*5*	*5*	*5*	-	-	*60*
Type-II									
Min	0.35	-	0.66	-	-	-	0.97	0.00	-
Max	7.73	-	0.97	-	-	-	1.00	0.03	-
Mean	4.38	-	0.87	-	-	-	0.99	0.01	-
N	*12*	-	*12*	-	-	-	*12*	*12*	-
Type-III									
Min	0.63	0.68	0.69	-	-	-	0.40	0.00	0.00
Max	26.28	0.97	1.06	-	-	-	0.87	0.14	0.57
Mean	6.44	0.77	0.92	-	-	-	0.68	0.03	0.20
N	*36*	*36*	*35*	-	-	-	*24*	*24*	*35*
Type-IV									
1	39.77	0.88	1.21	-	-	-	0.40	0.37	0.26
2	-	0.80		-	-	-	-	-	-
3	36.46	0.85	1.28	-	-	-	0.36	0.56	0.07
4	41.74	-	1.32	-	-	-	0.38	0.53	0.09

Table 5. Table summarising stable isotope data from the Gounkoto deposit and the surrounding area (for diagenetic pyrite). * - data points from Lawrence et al. (2013b). Abbreviations: Apy, - arsenopyrite, Ank – ankerite, Dol – dolomite, Hm – haematite, Mag – magnetite, Py – pyrite, Qtz – quartz.

	$\delta^{13}C_{PDB}$ (‰)		$\delta^{18}O_{SMOW}$ (‰)					$\delta^{34}S_{CDT}$ (‰)		$\delta^{18}O_{H2O}$ (‰)				
Sample	**Dol**	**Ank**	**Qtz**	**Dol**	**Ank**	**Mag**	**Hm**	**Py**	**Apy**	**Qtz**	**Dol**	**Ank**	**Mag**	**Hm**
Ore body														
JLS01	-	-	-	-	-	-	-	8.2	8.8	-	-	-	-	-
JLS02	-	-	-	-	-	-	-	7.0	-	-	-	-	-	-
JLS03	-	-	-	-	-	-	-	8.4	-	-	-	-	-	-
JLS05	-	-	-	-	-	-	-	9.5	-	-	-	-	-	-
JLS06	-11.2	-	-	19.1	-	-	-	10.0	-	-	14.0	-	-	-
JLS09	-	-	-	-	-	4.2	-	-	-	-	-	-	12.4	-
JLS10	-	-	-	-	-	-	-	6.4	-	-	-	-	-	-
JLS10B	-	-	-	-	-	-	-	7.8	-	-	-	-	-	-
JLS12		-13.6	12.9	16.3	-	-	-	12.5	-	7.3	11.2	-	-	-
JLS13	-	-	-	-	-	-	-1.3	-	-	-	-	-	-	8.7
JLS15	-	-	-	-	-	-	-1.5	-	-	-	-	-	-	8.5
JLS19	-	-	-	-	-	-	-	7.0	-	-	-	-	-	-
JLS20	-	-	-	-	-	-	-	9.7	-	-	-	-	-	-
JLS21	-	-	-	-	-	-	-	12.8	-	-	-	-	-	-
JLS22	-	-	17.1	-	-	-	-	5.9	-	11.5	-	-	-	-
JLS23	-	-	-	-	-	-	-	8.0	-	-	-	-	-	-
JLS25	-6.3	-	17.4	17.7	-	-	-	-	-	11.8	12.6	-	-	-
JLS26	-9.4	-	16.8	20.5	-	-	-	-	-	11.2	15.3	-	-	-
JLS27	-	-	-		-	-	-	9.6	-	-	-	-	-	-
JLS28	-6.7	-	16.1	15.2	-	-	-	-	-	10.5	10.0	-	-	-
JLS31	-	-	-	-	-	-	-	10.3	-	-	-	-	-	-
JLS33	-8.9	-	-	14.9	-	-	-	9.7	-	-	9.8	-	-	-
JLS34	-9.0	-	-	19.8	-	-	-	5.8	-	-	14.6	-	-	-
JLS34B	-	-	-	-	-	-	-	6.8	-	-	-	-	-	-
JLS35	-	-8.0	15.7	14.7	-	-	-	-	-	10.1	9.6	-	-	-
Diagenetic pyrite														
JLSB09	-	-	-	-	-	-	-	19.7	-	-	-	-	-	-
JLSB07	-	-	-	-	-	-	-	25.1	-	-	-	-	-	-
07YD52*	-	-	-	-	-	-	-	9.0	-	-	-	-	-	-
07YD89*	-	-	-	-	-	-	-	6.4	-	-	-	-	-	-
Barren carbonate veining														
JLS18	-2.4	-	-	18.2	-	-	-	-	-	-	-	-	-	-
JLS29	-0.5	-	-	18.2	-	-	-	-	-	-	-	-	-	-
Host dolostone														
JLS32	-3.1	-	-	19.3	-	-	-	-	-	-	-	-	-	-

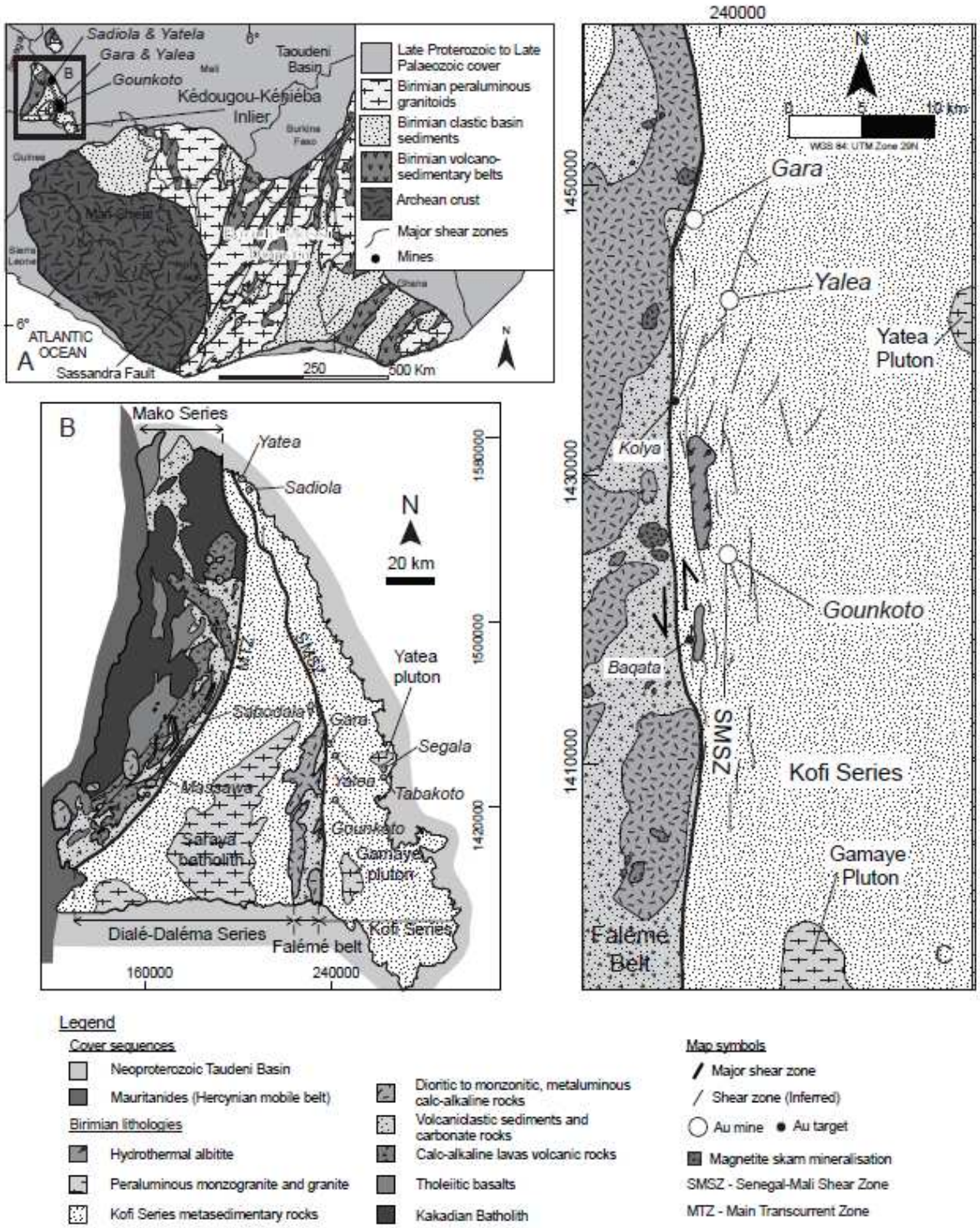

Fig. 1

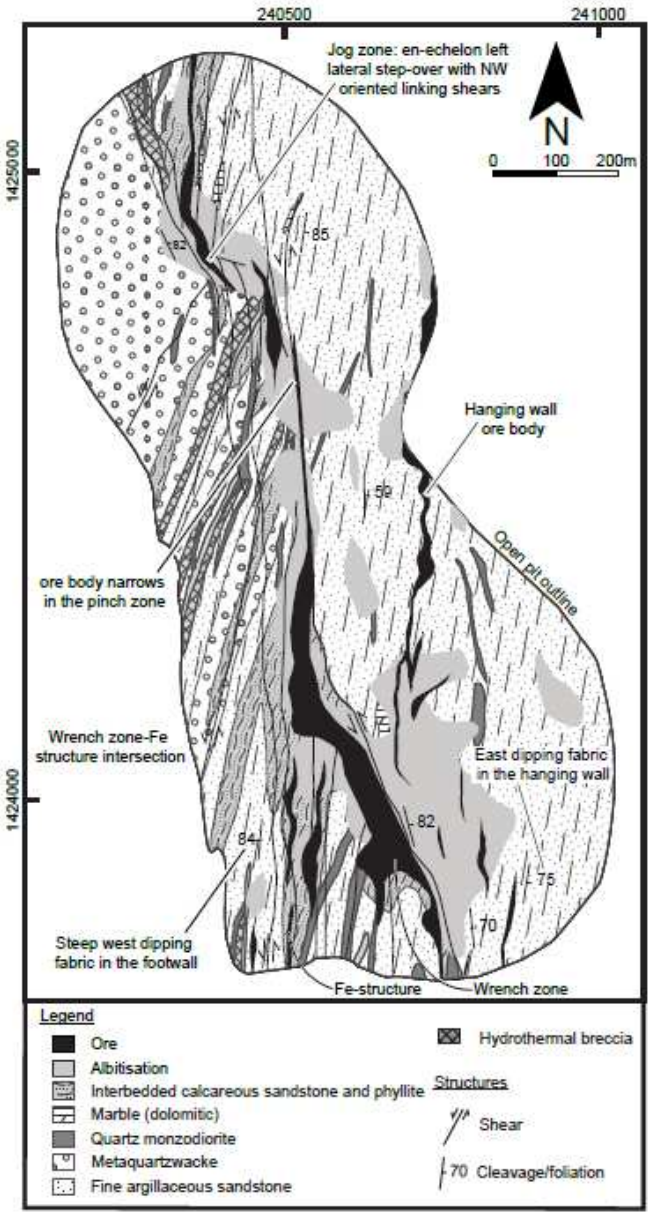

Fig. 2

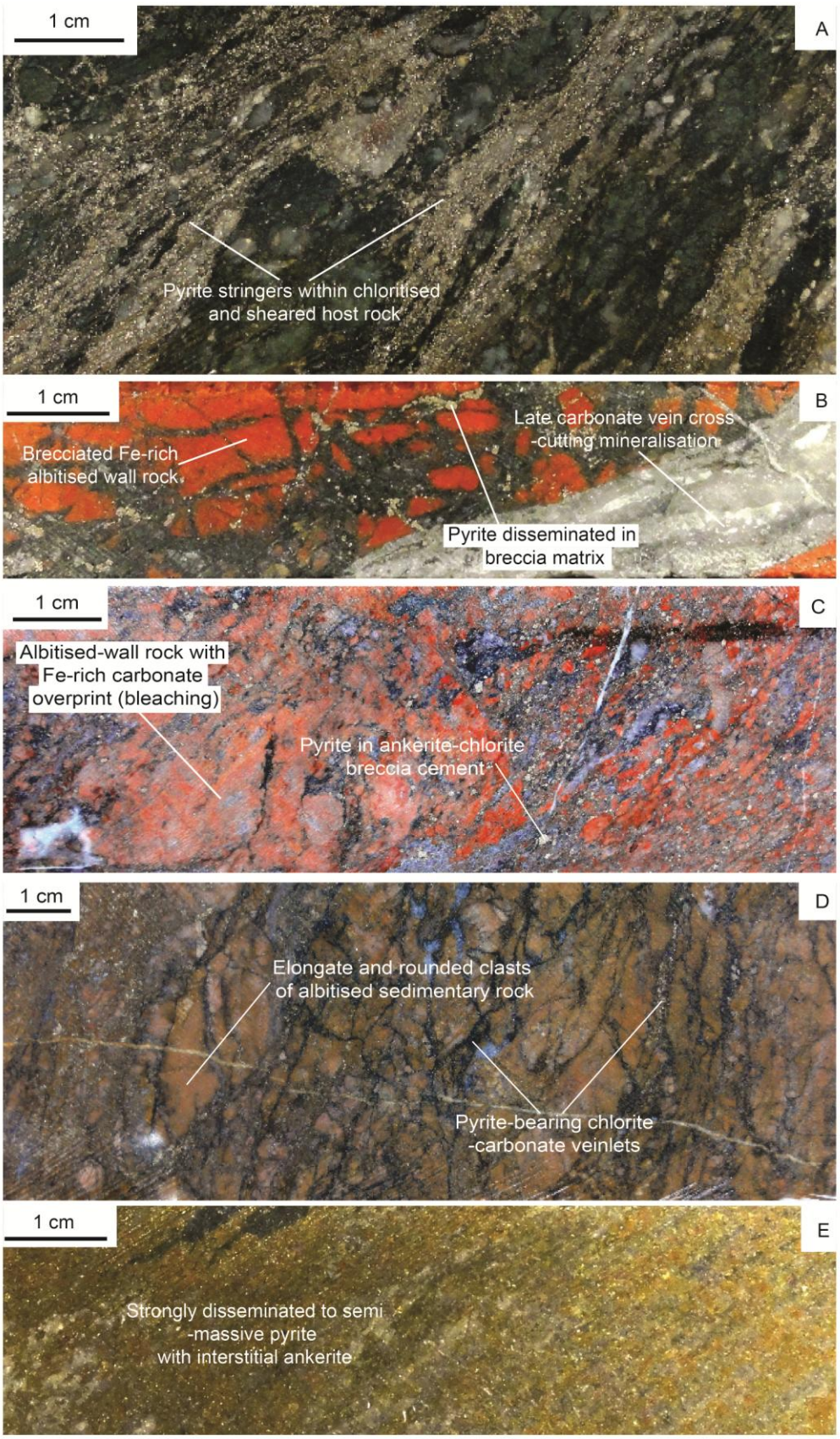
1 cm
A
Pyrite stringers within chloritised and sheared host rock
1 cm
B
Brecciated Fe-rich albitised wall rock
Late carbonate vein cross -cutting mineralisation
Pyrite disseminated in breccia matrix
1 cm
C
Albitised-wall rock with Fe-rich carbonate overprint (bleaching)
Pyrite in ankerite-chlorite breccia cement
1 cm
D
Elongate and rounded clasts of albitised sedimentary rock
Pyrite-bearing chlorite -carbonate veinlets
1 cm
E
Strongly disseminated to semi -massive pyrite with interstitial ankerite

Fig. 3

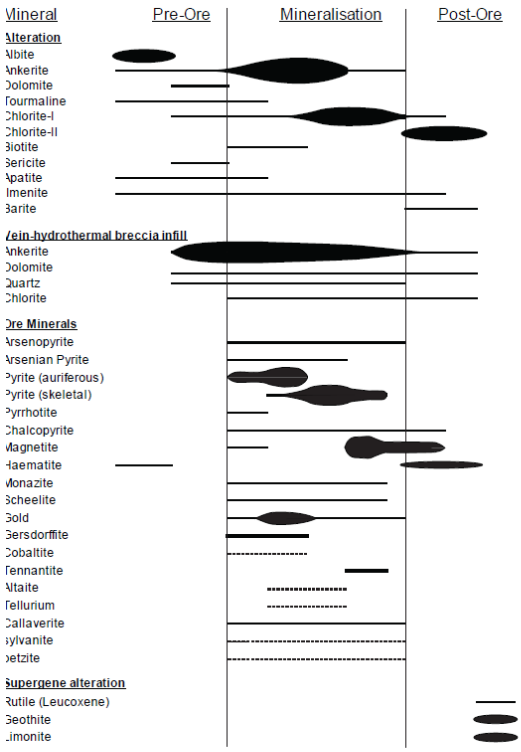

Fig. 4

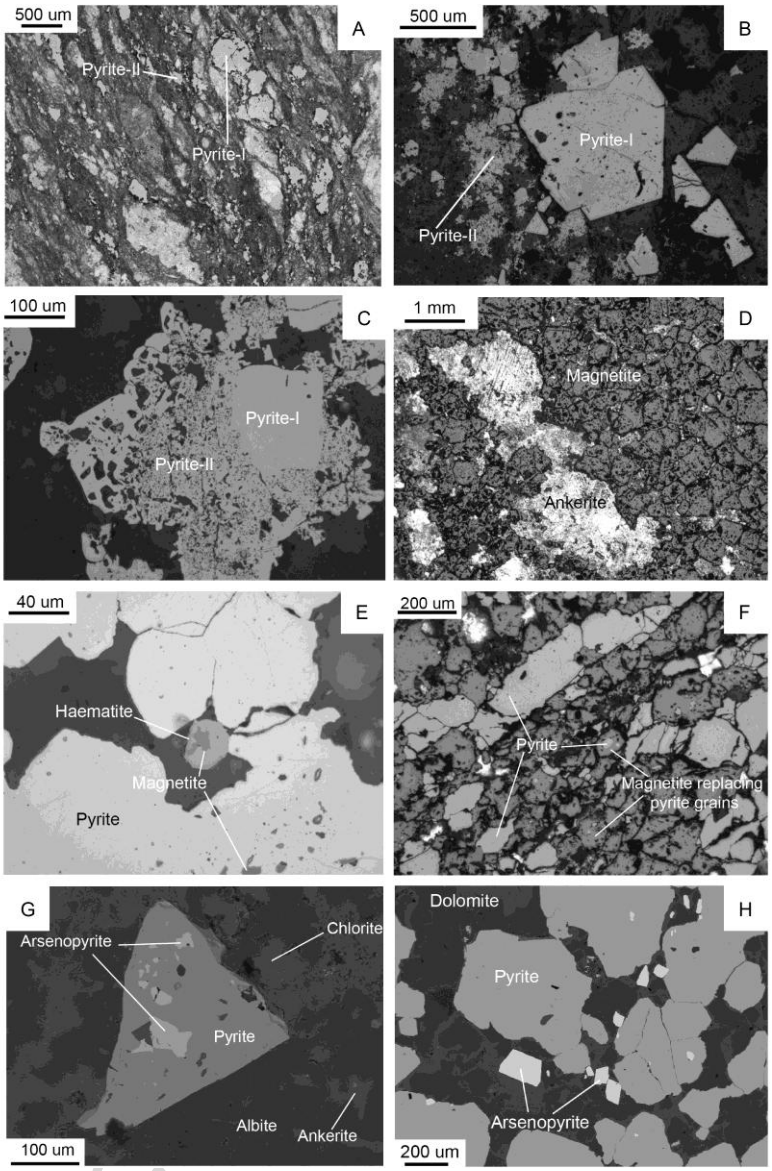

Fig. 5

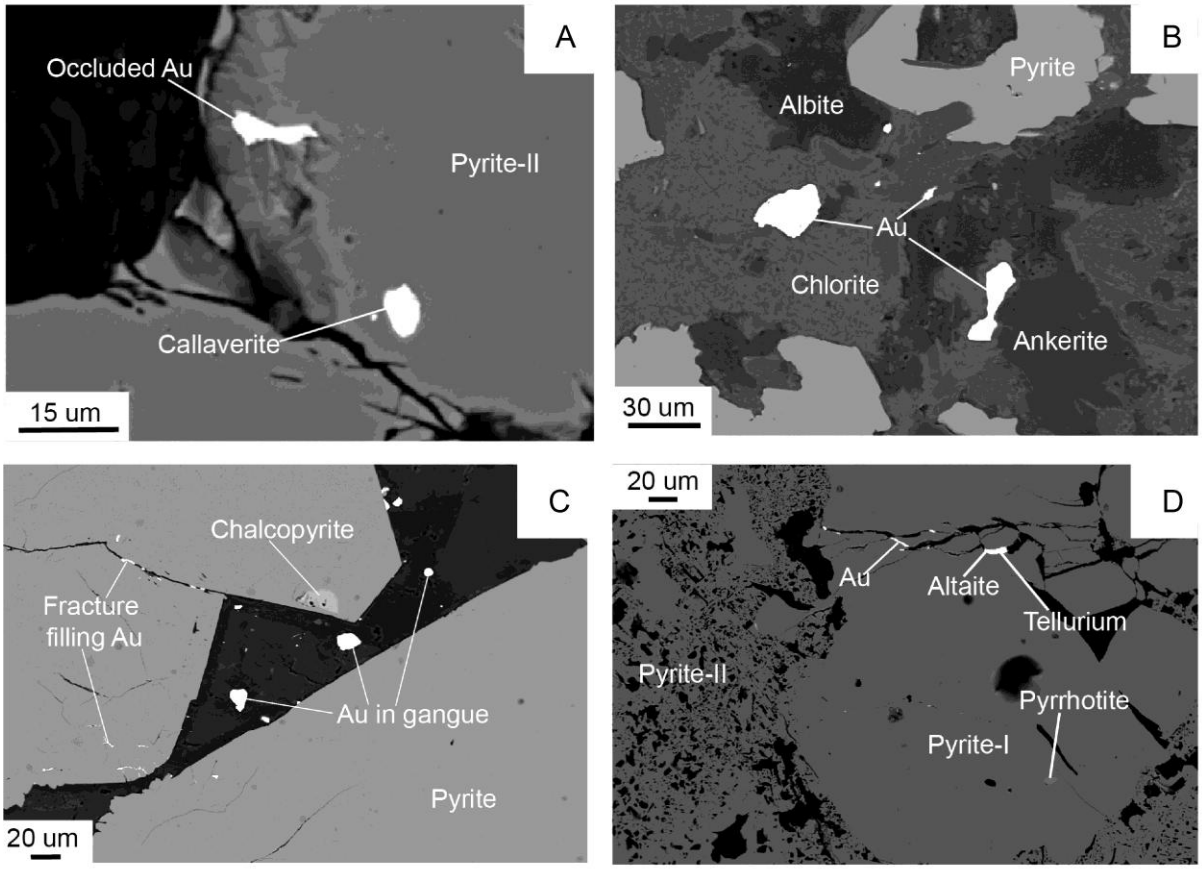
A
Occluded Au
Pyrite-II
Callaverite
15 um
B
Pyrite
Albite
Au
Chlorite
Ankerite
30 um
C
Chalcopyrite
Fracture
filling Au
Au in gangue
Pyrite
20 um
20 um
D
Au
Altaite
Tellurium
Pyrite-II
Pyrrhotite
Pyrite-I

Fig. 6

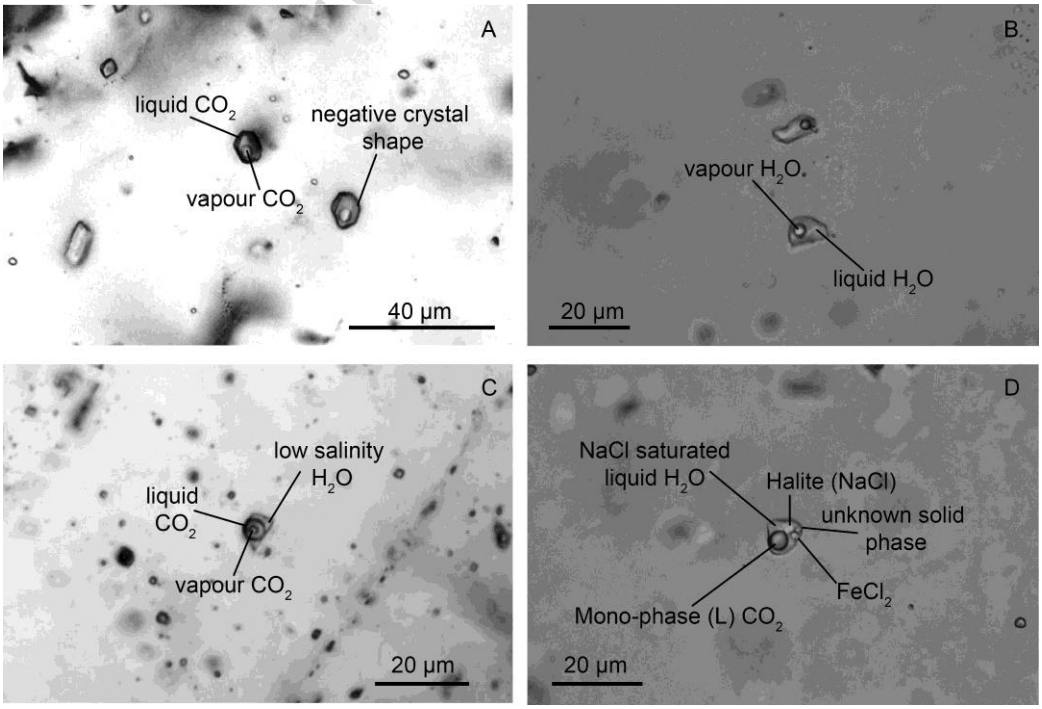
A
liquid CO_2
negative crystal
shape
vapour CO_2
40 µm
B
vapour H_2O
liquid H_2O
20 µm
C
low salinity
H_2O
liquid
CO_2
vapour CO_2
20 µm
D
NaCl saturated
liquid H_2O
Halite (NaCl)
unknown solid
phase
$FeCl_2$
Mono-phase (L) CO_2
20 µm

Fig. 7

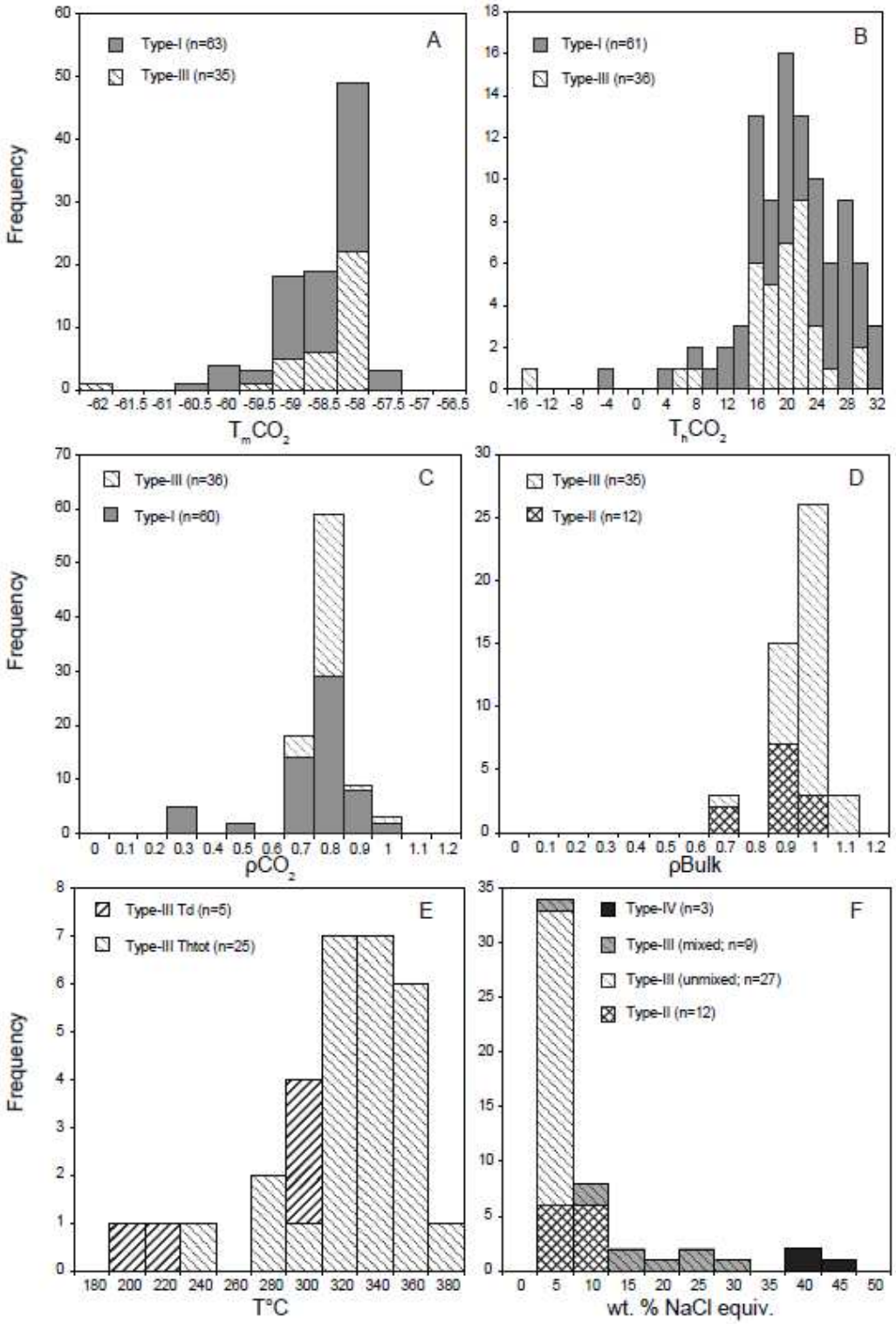

Fig. 8

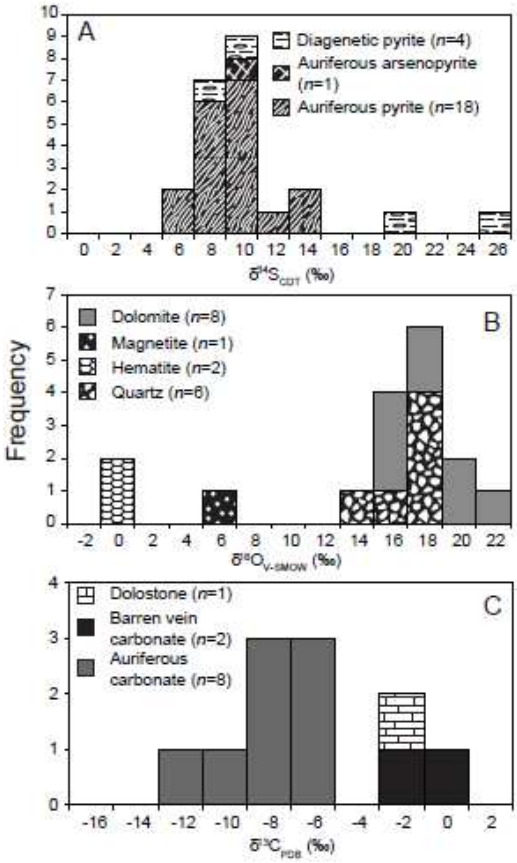

Fig. 9

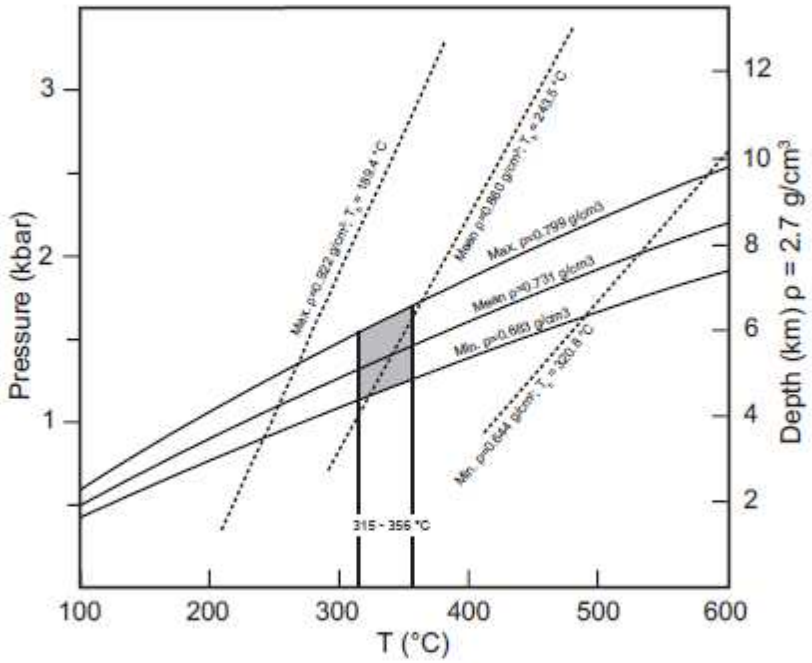

Fig. 10

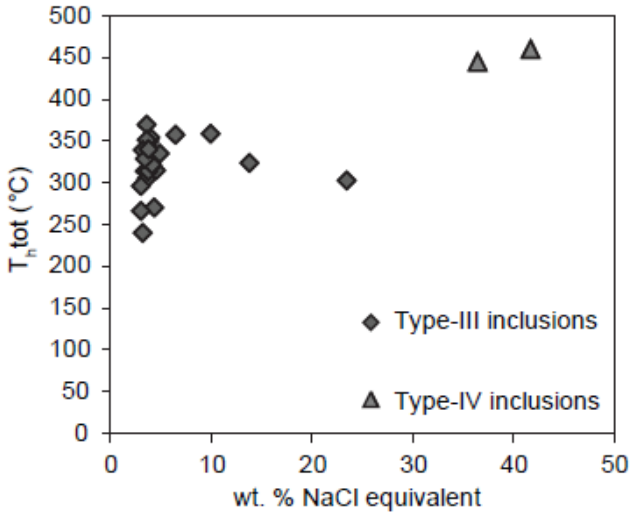

Fig. 11

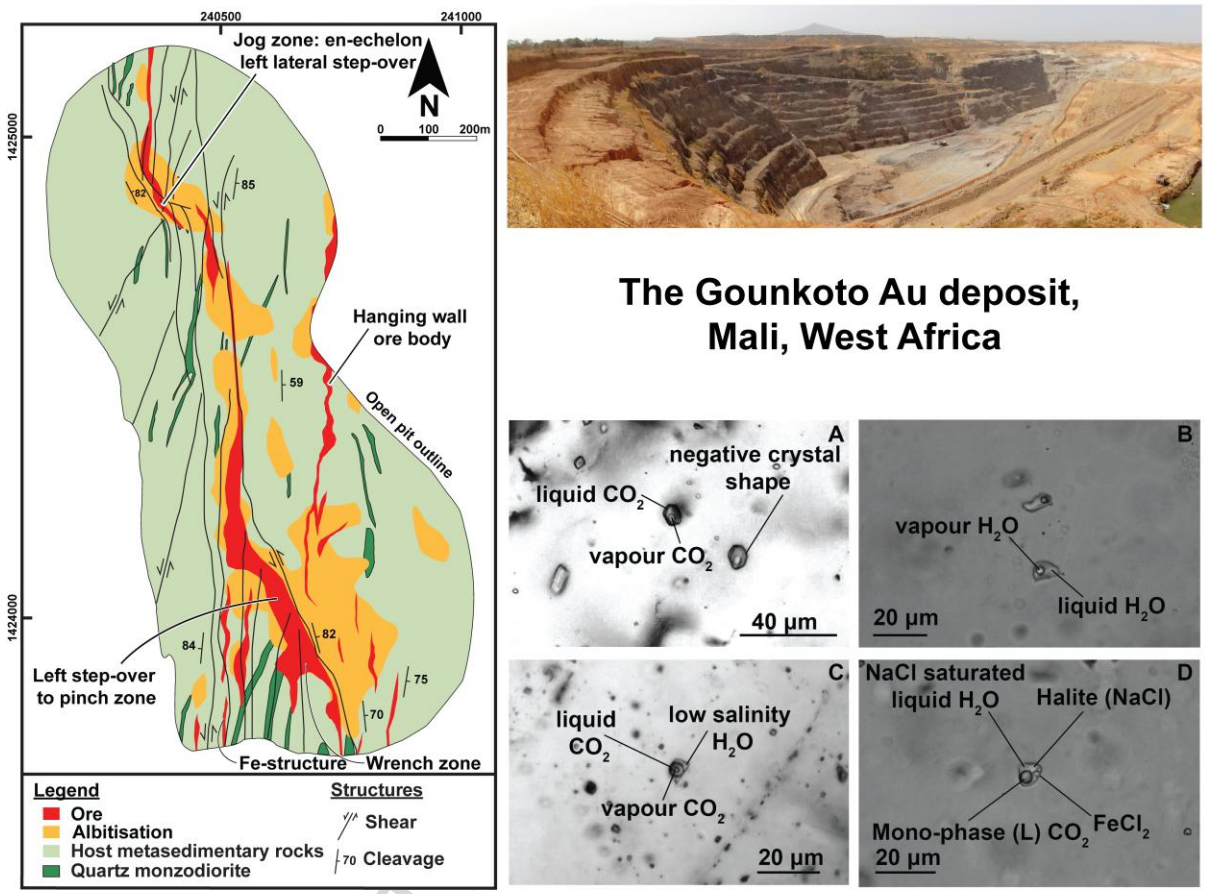

Graphical abstract

Highlights

- The Gounkoto ore body is characterised by sodic and phyllic alteration, As- and Fe-rich ore assemblages, with abundant magnetite, and overall enrichment in Fe-As-Cu-Au-Ag-W-Ni-Co-REE + minor Te-Pb-Se-Cd.
- Fluid inclusion assemblages indicate the presence of two hydrothermal fluids: (1) a moderate temperature (315-340 °C), low salinity (<10 wt. % NaCl equiv.), low density (≤1 gcm^{-3}), H_2O-CO_2-NaCl-H_2S±N_2-CH_4 fluid; (2) a high temperature (up to 445 °C), hypersaline (~40 wt. % NaCl equiv.), high density (~1.3 gcm^{-3}), H_2O-CO_2-NaCl±$FeCl_2$ fluid.
- These two fluids mixed during ore formation, leading to enhanced phase separation and Au precipitation.
- Fluid inclusion analysis indicate that the Gounkoto was formed at P-T conditions of approximately 1.4 kbar and 340 °C.
- Stable isotope analysis (O, C amd S) suggests that ore forming components were derived from devolatilisation of sedimentary rocks during metamorphism.